Department of Physics and Astronomy, University of Canterbury,
Private Bag 4800, Christchurch, New Zealand

The Atmospheric Gravity Wave Transfer Function above Scott Base

A Thesis Submitted in Partial Fulfilment
of the Requirements for a
Masters Degree in Physics
at the University of Canterbury

by

André Geldenhuis

University of Canterbury, 2008

Supervisors: Dr A. McDonald

Dr G. Fraser

Abstract

Gravity waves have a significant dynamic effect in the mesosphere. In particular, they drive the mesospheric circulation and are the reason that the summer polar mesosphere is cooler than the winter polar mesosphere. This thesis examines whether the effects of gravity waves are largely determined by filtering effects which allow only gravity waves with certain properties to propagate into the atmosphere. The filtering of gravity waves above Scott Base, Antarctica is examined using a radiosonde derived gravity wave source function, an MF-radar derived mesospheric gravity wave climatology, and a model derived filtering function. Least squares fitting of the source function and filtering function to the observed mesospheric gravity wave climatology allows us to determine which gravity wave phase velocities and propagation direction are likely to be present in the mesosphere and the relative importance of filtering and sources in this region. It is concluded the blocking of eastward gravity waves is important in winter and westward waves in summer.

Contents

List of Figures

Chapter 1

Introduction

"Despite the recognised importance of gravity wave processes to problems of general circulation, relatively little is known about their relative strengths and frequencies of occurrence" (*Nastrom and Fritts*, 1992). While progress has been made in the 15 years since this quote, the difficulties in observing these atmospheric features has not reduced its relevance.

1.1 Motivation

Gravity waves have been theorised to exist since Lord Rayleigh first considered stability effects in the atmosphere. Indeed, early work with meteor radar and radiosondes made measurements of relatively rapid perturbations to the background flow. *Hines* (1960) clearly notes that these winds could be due to internal gravity waves propagating from the troposphere and growing exponentially with height. In the early 1980's, several papers were published suggesting that gravity waves could play a significant role in mesospheric dynamics through the transport of momentum from the lower atmosphere (see *Lindzen*, 1981; *Holton*, 1982).

The understanding of the particular importance of gravity waves came at a fortuitous time, as recent developments by University of Canterbury researchers at the Birdlings Flat site had lead to the use of MF-radar to measure winds through the observation of radar backscatter from partial ionisation in the D-region of the atmosphere (*Fraser*, 1984a). While MF-radar had been used to determine mesospheric winds prior to this, the use of radar backscatter allowed measurements to be taken of winds at lower altitudes than previous full reflection methods allowed. At lower altitudes the collision frequency between the ionised and neutral gas is sufficiently high that the ionised gas velocities can be assumed to be representative of the neutral gas velocity.

While the field of gravity wave study has matured since its early days, there are still a great many areas in which more research is needed. During a gravity wave conference in 2006, several areas where an improvement in understanding of gravity waves was needed were highlighted. One of these areas was that of gravity wave sources and propagation (*Geller et al.*, 2006). For this reason, this thesis aims to provide a greater understanding of gravity wave sources and propagation above Scott Base, Antarctica, and their relative importance

on the observed mesospheric gravity wave field.

1.2 Structure

The following two chapters of this thesis give a general overview of atmospheric dynamics and structure, and gravity wave theory.

Chapter 4 uses data from the Scott Base MF-radar, run by the University of Canterbury. Recently, this radar was upgraded to improve its ability to resolve gravity waves above the background noise level (*Baumgaertner et al.*, 2006). In order to resolve gravity waves, atmospheric tides and larger scale perturbations are removed from the wind data. The variance of these perturbations is taken to be due to gravity waves. Using this method, a gravity wave climatology is produced which spans the years after the radar upgrade, from 2005 to early 2008.

Chapter 5 details the use of radiosondes launched from McMurdo (which is very close to Scott Base) to determine a gravity wave source function. This source function takes the form of a climatology of kinetic energy due to gravity wave perturbations. Unfortunately, there was a significant change in the McMurdo radiosonde program in late 2004, which, combined with the public availability of the McMurdo radiosonde data set ending in 2007, left little more that two years of good data. To discern the effect of using such a small data set, a gravity wave climatology for the years before the program change was also calculated covering 2000 - 2004. Comparing the mean kinetic energy before and after the change, it was determined that the post-upgrade data was sufficiently representative to be used as a gravity wave source function.

Chapter 6 uses wind data from the Horizontal Winds Model 93 (HWM 93) to develop a gravity wave filtering function model based on critical level filtering and blocking circles. This atmospheric transfer function is calculated for several ranges of potential gravity wave phase speeds and propagation directions. The transfer function indicates the degree to which gravity waves with certain properties (such as phase speed and propagation direction) are blocked as they move up through the atmosphere.

Chapter 7 combines the atmospheric transfer model, the gravity wave source function and the MF-radar observed gravity wave climatology, to determine the importance of the filtering of east and west propagating gravity waves to the observed gravity wave field. Finally, Chapter 8 summaries the overall content and discusses the results, offering possible explanations and ideas for future research.

Chapter 2

Atmospheric Dynamics

2.1 Structure

At the broadest scale, the structure of the Earth's atmosphere varies horizontally from the equator to the poles. These variations are due to different energy deposition rates and the Coriolis Effect.

The vertical variations are similar enough over the globe that the changes in temperature gradient as a function of height are used to identify different regions of the atmosphere. Based on these changes in temperature gradient (or lapse rate), the atmosphere can be divided into several different altitude regions, shown in Figure 2.1. The first is the troposphere, starting from the ground and extending to approximately 10 -15km. This region is warmed primarily by heat radiating from the ground and cools increasingly with altitude as clouds and water vapour radiate heat into space (*Andrews et al.*, 1987). The cooling trend in the troposphere makes it almost dynamically unstable; moist rising air masses can remain warmer than the surrounding air due to water droplets condensing and releasing their latent heat into them. Since the air mass is warmer than its surroundings it can continue to rise, causing this region to be well mixed.

The variation in solar heating from the equator to the poles results in horizontal temperature gradients. This gradient forces air masses away from the equator. However, as the equator is further from the planet's axis of rotation, these air masses posses greater angular momentum than they would at higher latitudes. As such, conservation of angular momentum dictates that as air masses move eastward (prograde), they also try to move toward the poles. This results in the eastward tropospheric jets used by airlines to decrease travel times on eastward-bound flights. Because the tropospheric equator is always warmer than the poles, these jets move to the east regardless of the season.

At greater altitudes the low temperatures reduce the amount of water vapour that the air can contain. Above the troposphere the atmosphere is very dry, and warms increasingly with altitude. The change from cool to warm air and the very low humidity are signatures of the stratosphere. This warming is due to the rapid rise in ozone above the tropopause. Ozone strongly absorbs UV light, depositing energy into the stratosphere. The amount of ozone peaks in the lower stratosphere. However, temperature continues to rise with altitude

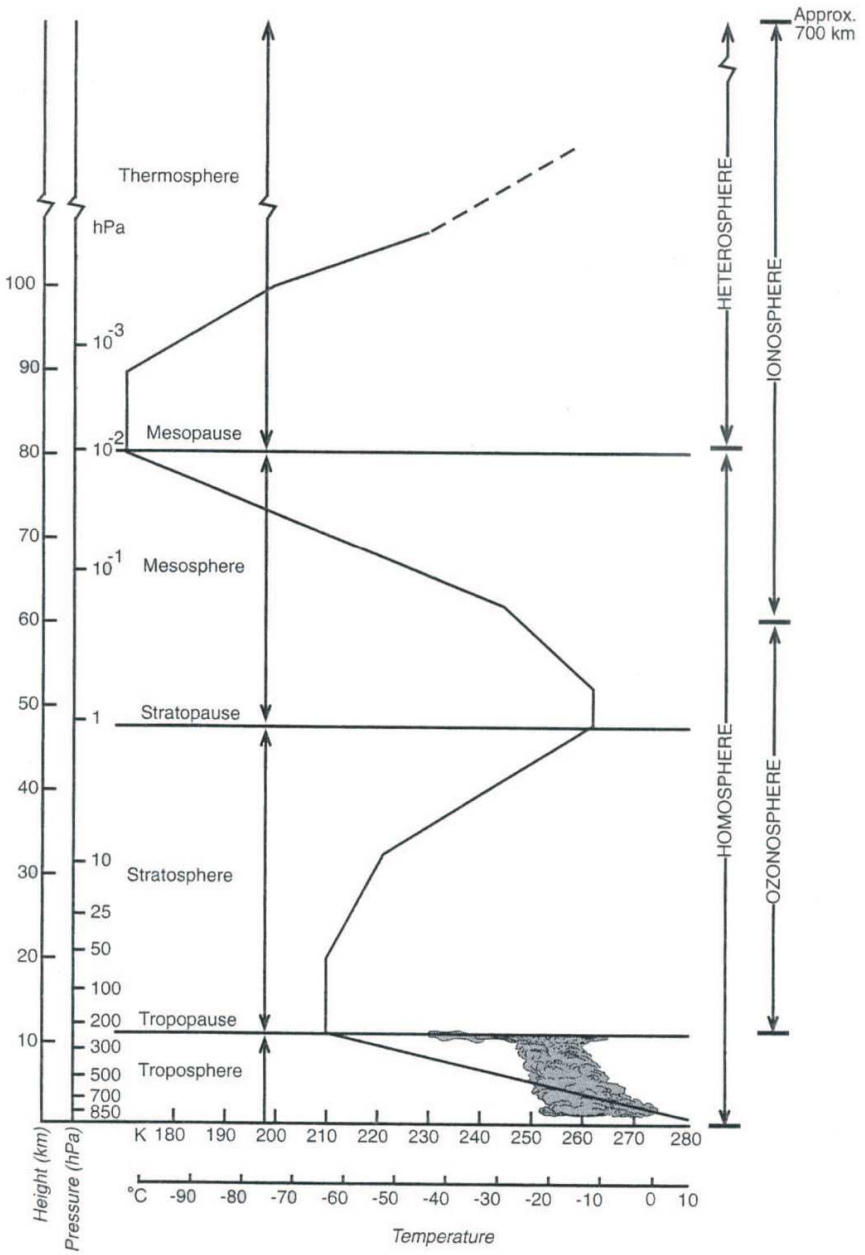

Figure 2.1: Vertical structure of the atmosphere. (*Sturman and Tapper*, 2006)

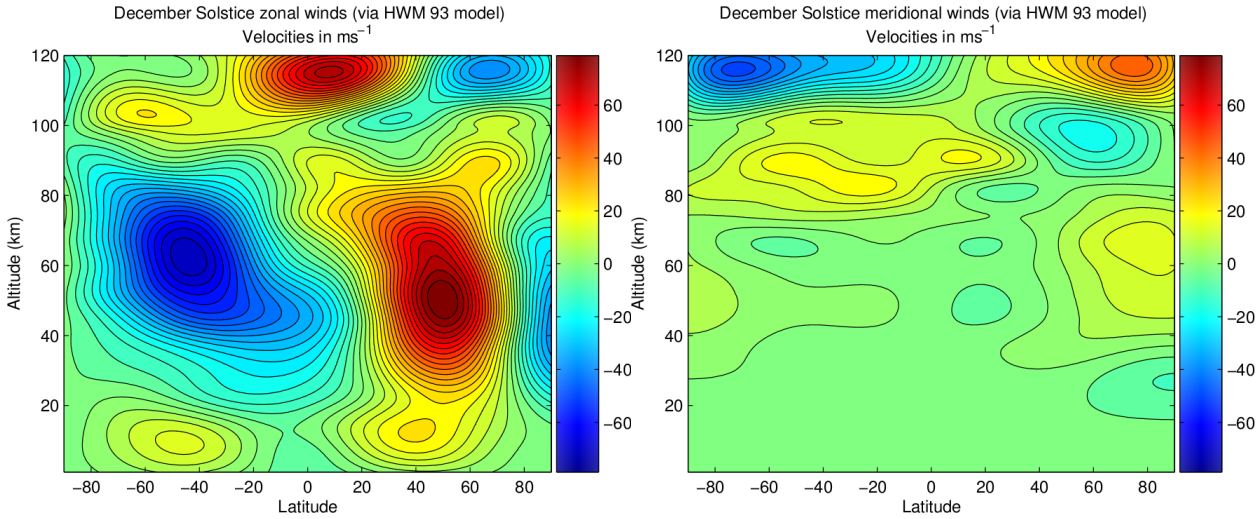

Figure 2.2: Zonal and meridional winds during the December solstice using HWM 93 model data. The zonal winds divides quite naturally into 3 layers: The lower atmosphere from approximately 0-20km, the middle atmosphere (encompassing both the stratosphere and mesosphere) from roughly 20-80km, and the upper atmosphere above 80km.

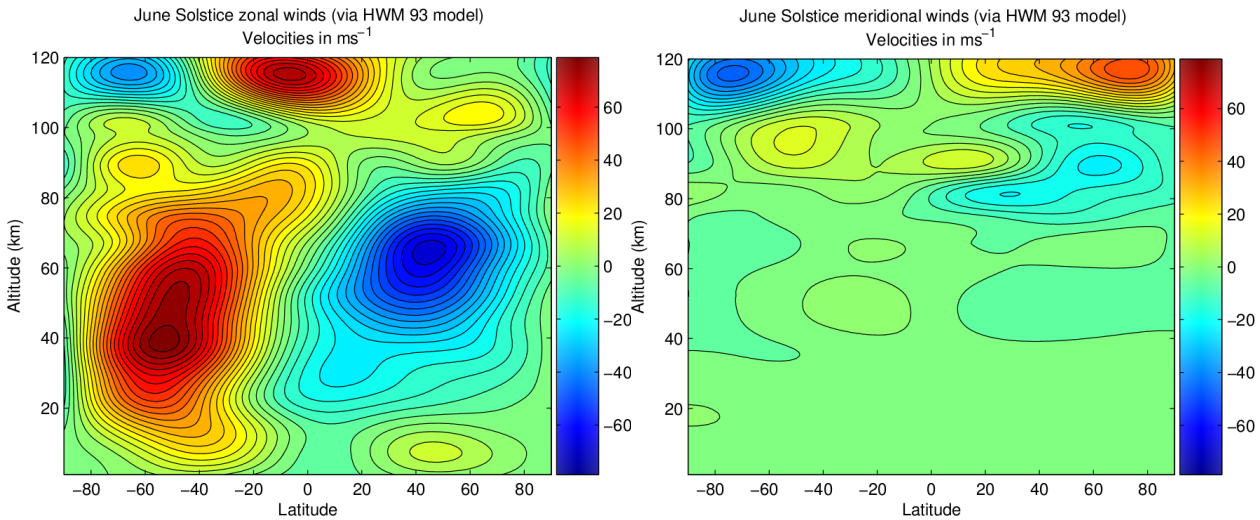

Figure 2.3: Zonal winds during the June solstice. Note that the stratospheric summer jet is in the westward direction.

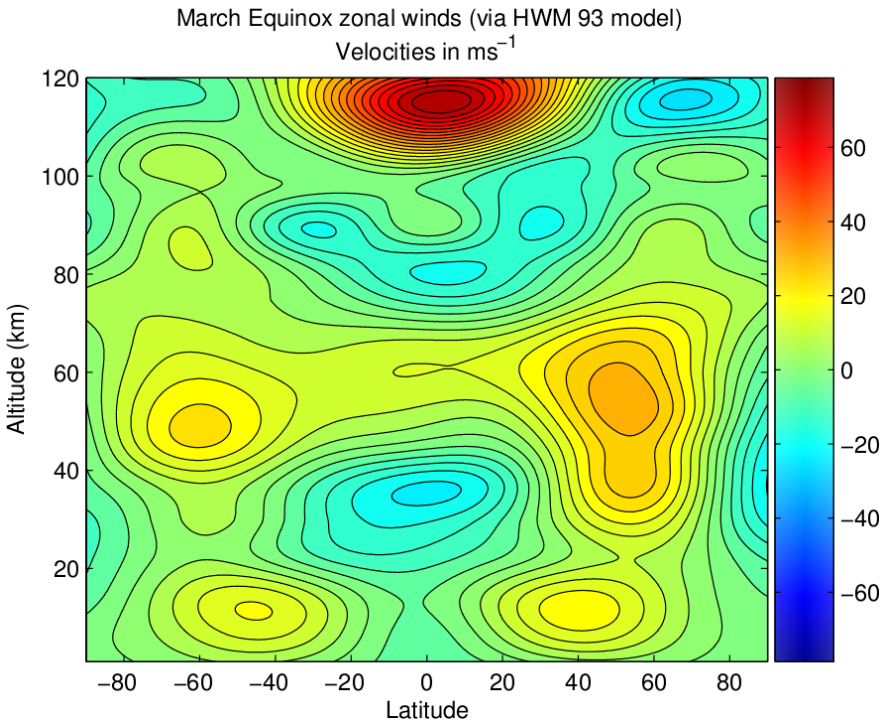

Figure 2.4: Zonal wind velocities during the March equinox. In this configuration, the sun heats the equatorial stratosphere more than the pole, causing the middle atmosphere jets to both blow east.

due to decreasing atmospheric density (requiring less energy to heat).

This heating by ozone-absorbing UV light is the primary warming mechanism in the stratosphere. This leads to some interesting differences to the tropospheric region. Since the summer pole receives far more irradiance than the equator, the high latitude summer stratosphere is warmer than the equatorial stratosphere because of radiative heating. This leads to a reversal of the summer stratospheric jet. Due to conservation of angular momentum, as air masses attempt to move toward the equator they will appear to to be forced toward the west, resulting in a westward (retrograde) summer jet. The equatorial stratosphere is still warmer than the winter stratosphere at this height, hence the winter jet is eastward, similar to the tropospheric jets (see Figure 2.4).

The temperature trend in the stratosphere makes it very stable. Any vertically displaced parcels of air will attempt to return to its equilibrium position, oscillating until damped. This oscillation makes the stratosphere an excellent medium for the propagation of gravity waves, which will be discussed in the next chapter.

Above about 50km the ozone concentration drops and the temperature decreases due to the absorption of UV light. This cooling point leads into the atmospheric region known as the mesosphere. A particularly notable feature of this region is that it also encompasses the D-region of the ionosphere. *Nicolet and Aikin* (1960) discuss the formation of the D-region in some detail. They indicate that several atmospheric species in this region are ionised by Lyman-α radiation from the sun as well as X-rays and cosmic rays. However, the ionisation in this region is fairly weak and recombination of ionised species occurs fairly quickly. As such, this region is dominated by the neutral species. This is useful as it allows partial radar reflections and yet is still to all intents and purposes neutral and unaffected by the Earth's

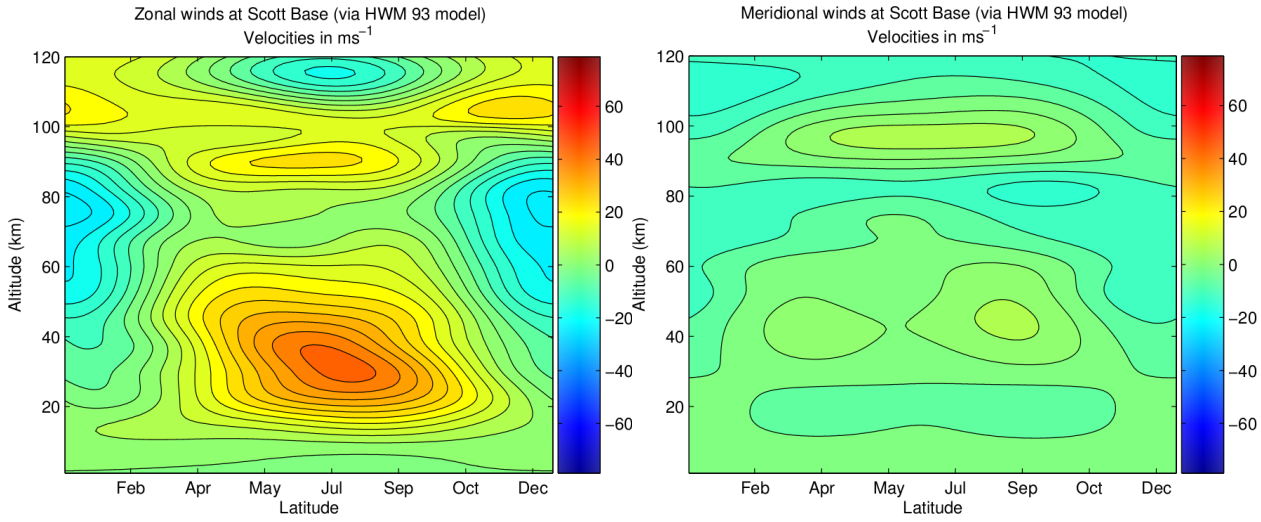

Figure 2.5: Zonal and meridional winds at Scott Base via the HWM 93 model.

EM field. Another interesting feature of this region is that at high latitudes the winter mesosphere is *warmer* than in summer. This has been attributed to the action of breaking gravity waves (*Geller*, 1983).

The final region considered in this thesis is the lower thermosphere. This region begins where the temperature starts to increase above the mesopause at around 85km. The temperature increase in this region is due to the absorption of high energy UV radiation from the sun (*Kelley and Heelis*, 1989). As the electron density due to ionisation grows quickly in this region, this thesis will confine itself to altitudes of $96km$ and below where electromagnetic effects on the plasma in this region can be considered to have an insignificant effect on the motion of the neutral component of the atmosphere.

2.2 Atmospheric waves

Atmospheric waves play a significant role in the dynamics of the atmosphere. They are particularly important in coupling different regions together. The action of large scale planetary waves is the mechanism by which tropical convection can influence extra tropical dynamics (*Salby*, 1996). Indeed it shall be shown in the following chapter that short period atmospheric waves (internal gravity waves) can provide coupling between the troposphere and the mesosphere, driving the dynamics in the latter region.

The largest-scale atmospheric waves are the planetary waves and Rossby waves which have diverse effects on the atmosphere. These waves can transport heat and momentum to high altitudes which is released by wave breaking. For instance, it has been demonstrated that the breaking of these large scale waves can decelerate the polar vortex leading to the vortex breakup up earlier in the season (*Holton and Alexander*, 2000).

Another type of large scale wave are atmospheric tidal waves. These waves are generated via several mechanisms, the most significant is solar heating (*Chapman and Lindzen*, 1970). The tidal modes considered in this thesis are harmonics of the solar driven diurnal tide.

Lastly, internal gravity waves are shorter period waves that are present throughout the

atmospheric column. These wave are subject to filtering by winds as they propagate through the atmosphere. This filtering process of internal gravity waves is the focus of this thesis, and it is used to produce an atmospheric transfer function for gravity waves of various phase speeds above Scott Base. These waves and their effects are detailed in the following chapter.

Chapter 3

Gravity Waves and Observational Techniques

"Despite the recognised importance of gravity wave processes to problems of general circulation, relatively little is known about their relative strengths and frequencies of occurrence" (*Nastrom and Fritts*, 1992).

3.1 Gravity waves

Waves with the restoring forces of gravity and buoyancy are known as gravity waves. These waves are present through much of the atmosphere with periods between the Brunt-Väisälä period and inertial period.[1] There are many mechanisms by which these waves can form; however, the gravity waves above Scott Base (which are examined in this study) are likely to be predominantly formed by winds passing over the Trans-Antarctic mountain range (*Baumgaertner and McDonald*, 2007). As the air passes over the ranges it is displaced from its equilibrium position and oscillates around this height position as it moves down-wind of the mountain, creating a wave. The air column above is also displaced, allowing the gravity wave to propagate almost vertically well into the thermosphere.

These waves provide much of the coupling between the lower and upper atmosphere by transporting energy to higher altitudes[2]. This is particularly important in the Antarctic MLT, as this is the region of the atmosphere farthest from radiative equilibrium (*Gill*, 1982). For example, the winter temperature in the MLT above the polar regions is generally higher than that in summer. While at first glance this observation may appear unexpected, it has been shown to be related to the forcing associated with gravity waves. The energy transported by gravity waves has also been shown to control the strong mesospheric winds and play a significant role in closing the stratospheric jets(*Lindzen*, 1981; *Holton*, 1982).

The stratospheric jets define the polar vortex, the strength of which determines the degree of mixing between the Antarctic and the mid-latitude stratosphere (*Krutzmann et al.*, 2008). The degree of mixing therefore plays an important role in ozone dynamics. As such,

[1] infinite at equator to 12 hours at poles(*Fritts and Alexander*, 2003)

[2] (See *Hamilton* (1999) for an overview of the discovery of this phenomena)

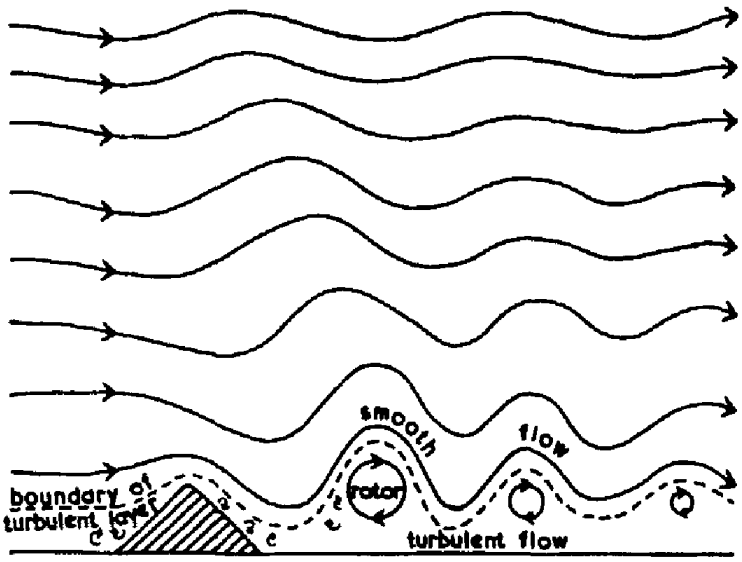

Figure 3.1: Topographically generated gravity waves. Adapted from *Gerbier and Berenger* (1961).

the study of internal gravity waves in the Antarctic atmosphere is important to further our understanding of these phenomena.

3.1.1 Sources of gravity waves

There are a variety of gravity wave sources in the atmosphere, while some of these sources are not significant in the Antarctic, the main sources shall be briefly detailed below.

Perhaps the most easily understood source of gravity waves is topographic generation. As wind blows over a mountain range packets or parcels of stable air are vertically displaced. As these parcels move downwind from the mountain range, they seek to return to their equilibrium position due to the effect of gravity as they are denser than the surrounding atmosphere. However they tend to overshoot this position at which point the force of buoyancy acts to reverse their motion as they are now less dense than the surrounding medium. This process is illustrated in Figure 3.1. A notable property of mountain waves is that their phase speed is locked to the topography below. This will be shown to be particularly important when wave breaking and wave drag are considered.

Another source of gravity waves is geostrophic adjustment around jets. Large scale movements of the atmosphere tend to remain in balance with all the forces that would act on them, as this is the lowest energy state. However, as the atmosphere is a dynamic environment with many competing effects, these large scale motions are often not in balance.This can be the case around jets in the atmosphere as their large scale enables them to alter the geostrophic balance of the atmosphere. (*de la Torre and Alexander*, 2005). A return to the lowest energy state, in this case termed geostrophic adjustment, requires the radiation of energy. In the atmosphere this energy is radiated away in the form of gravity waves.

Strong wind shear can generate Kelvin-Helmholtz instabilities along the shear line or shear envelope. As this instability returns to the low energy original state, it radiates gravity

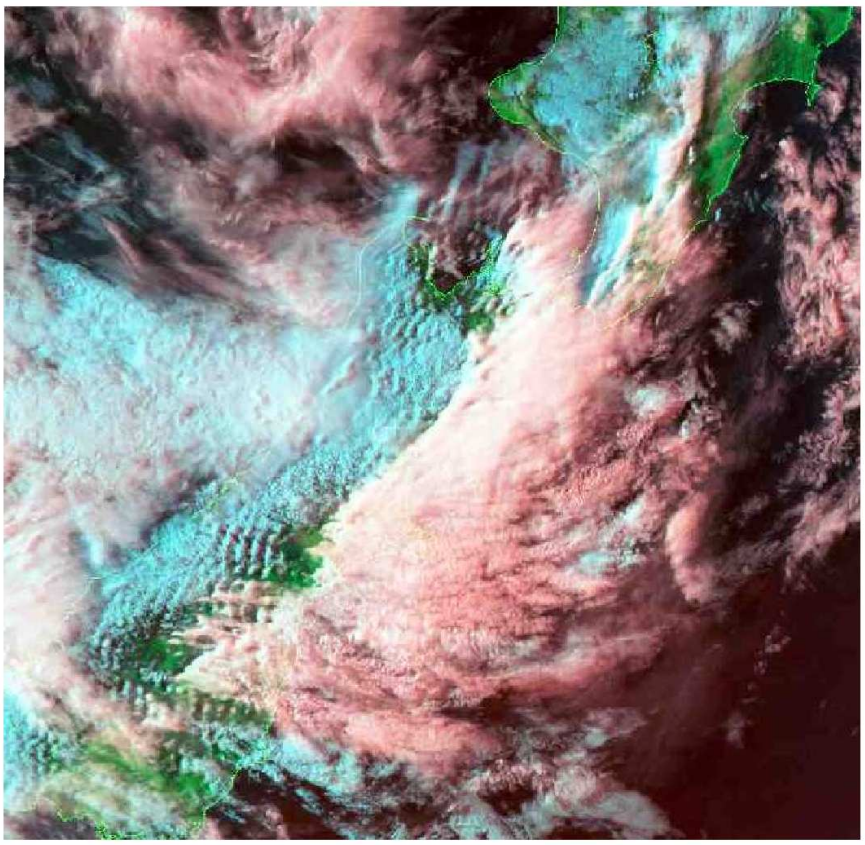

Figure 3.2: An image from the NOAA-14 satellite on the $4^{th}$of October 1999. Taken from *Dean* (2002)

waves away – though the actual mechanism is non-linear (*Buhler and McIntyre*, 1999). Both wind shear and geostrophic adjustment radiate gravity waves with phase speeds similar to the wind speed with which they are associated (*Sutherland and Peltier*, 1995).

Strong convection is another mechanism which can produce gravity waves (*Fritts and Alexander*, 2003). However, the Antarctic is too cold for any significant convective activity so this gravity wave source shall not be considered in this thesis.

3.2 Observation methods

Gravity waves can be observed in a variety of ways. At the simplest level, gravity waves can occasionally be seen as lee clouds when wind flows over a mountain range. There are a variety of more sophisticated optical observational methods, ranging from air-glow images taken at night, to satellite images of clouds associated with gravity waves (see Figure 3.2). Satellite-based instruments are also able to obtain temperature profiles, often by limb sounding or radio occultation techniques. These temperature profiles can be used to determine larger-scale gravity wave activity.

Prior to the satellite era, the only way to sample a wide range of altitudes was by using sounding rockets (*Goldberg*, 1986). Even after the advent of atmospheric satellite data, rockets have been used for both high-resolution studies applicable to gravity waves and

verification of satellite results.

The two techniques that this thesis uses to acquire gravity wave data are MF-radar and radiosondes. These two techniques are presented in more detail below.

3.2.1 Scott Base MF-radar

The Scott Base MF-radar measures horizontal winds in the mesosphere and lower thermosphere (MLT). The radar transmits pulses which are partially reflected from the D-region of the ionosphere, and produce diffraction patterns which can be observed at the ground. The radar measures wind speeds by analysing the movement of these diffraction patterns using a set of spaced receiving antennas. In the following chapter, the atmospheric tidal signals are removed from this wind data in order to identify the wind perturbations due to gravity waves alone, albeit with some degree of noise.

The Scott Base MF-radar consists of the transmitter at Scott Base, Antarctica ($77°51'S$, $166°45'E$) and a spaced receiving array at Arrival Heights 3.3km away (*Fraser*, 1984a). The radar operates at a frequency of 2.9Mhz, with a peak power of 100kW. The transmitter currently has a pulse repetition frequency of 30Hz, although it has been lower in the past (*Baumgaertner et al.*, 2006; *Fraser*, 1984b).

The transmitting antenna and three receiving antennas are all deltas (triangular antennas). Because delta antennas have an almost isotropic radiation pattern they are not optimal for observing the atmosphere above the radar.[3] However, deltas have been shown to be more resistant to wind and ice stress problems (*Fraser*, 1984b), which is particularly important in the Antarctic where antenna maintenance can be a daunting task even during the relatively mild summer months.

The transmitting antenna is a single, open-wire delta located very close to the Transmitter Hut which is short walk from the Hatherton Laboratory. The receivers are located at the new Arrival Heights Laboratory with the antennas spaced near by. The three antennas which comprise the receiving array are arranged in an equilateral triangle with spacing between their phase centres approximately 125m apart. Snow flakes carry a static charge which manifests as receiver noise and therefore the receiving antennas are insulated to prevent this.

The signal of interest that is returned from the atmosphere is a partial reflection of the radar waves caused by variations in the radio refractive index of the atmosphere. These variations are due to electron density increasing with altitude and horizontal variations (*Manson and Meek*, 1984). The horizontal variations are of the correct scale for Fresnel diffraction of the backscatterered radar wave to occur, which produces a diffraction spot on the ground.

Assuming that the horizontal variation in electron density moves with the background wind, the movement of the diffraction pattern at the surface will be directly related to the winds at the reflection altitude. However, since electrons are required in order to produce the diffraction pattern, the assumption that the variations are moving with the background

[3] If the antenna pattern is directed upward, this has the dual effect of increasing the system's gain as well as rejecting noise from the horizon. Graham Fraser, p.c.

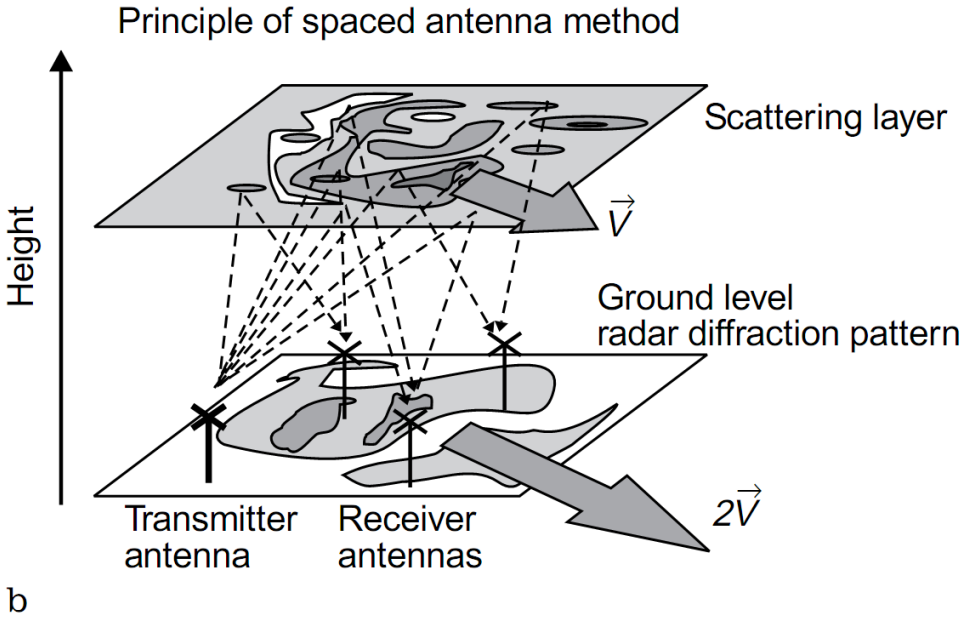

Figure 3.3: Spaced array techniques (*Hocking*, 1997). Radar is backscattered producing a Fresnel diffraction spot on the ground. The equilateral triangle of receiving antennas allows the velocity of the diffraction spot to be measured, this corresponds to the movement of the scattering layer.

wind is only valid when electrons are colliding frequently with neutral atoms. At altitudes higher than 95 to 100km, the collision frequency is low enough that the electrons become increasingly affected by geomagnetic effects and this assumption is no longer valid (*Fraser*, 1984b). Therefore, the radar winds were taken from an altitude range of 75 to 96km.

To determine the horizontal wind speed, the movement of the diffraction spot is observed by the three receiving antennas. Each antenna detects a portion of the diffraction spot. There are two methods by which the antenna and associated receiver do this: the least complicated method is to use a simple amplitude receiver, which measures the contours simply as changes in received signal strength. A more sophisticated method uses phase-sensitive receivers to obtain more information about the returned signal. For simplicity, only the amplitude changes method will be described. Note that most modern MF-radars (such as the radar at Scott Base) use these phase-sensitive receivers although the basic concepts are applicable to both.

As a diffraction spot moves over the receivers (see Figure 3.3) it produces changes in the amplitude of the received signal. If there were many more than three receiving antennas, it would be simple to track the motion of the diffraction spot since it could effectively be imaged. However, the motion of the diffraction spot can still be determined even with only three antennas.

As the variation in received signal moves over each antenna, its shape is recorded, represented by the contours in Figure 3.3. Assuming its shape does not change, as the diffraction spot moves over the other antennas the recorded signal will bear similarities to the signal received at the first antenna. This is shown schematically in Figure 3.4; as the diffraction spot moves over successive receivers, it is displaced in time and changes somewhat. The signals

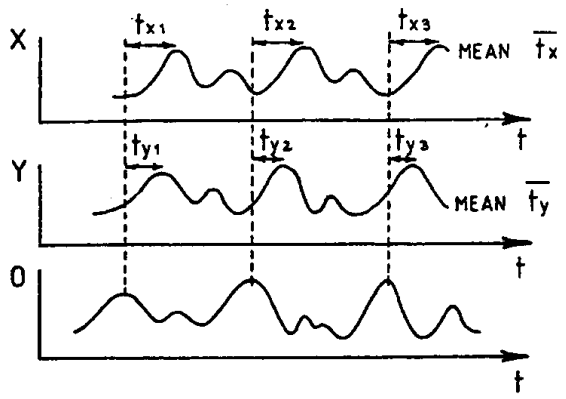

Figure 6.

Figure 3.4: Amplitude of a Fresnel diffraction spot moving over three antennas. From *Briggs* (1984).

at different receiving points can then be compared using a technique called Full Correlation Analysis (FCA), which is clearly detailed in *Briggs* (1984).

Currently the Scott Base MF-radar takes measurements for one minute while the FCA algorithm is run on the previous minutes data. The FCA algorithm is used to calculate horizontal winds from $60km$ to more than $100km$. As most of the mechanisms responsible for ionisation in the D-region of the ionosphere are due to sunlight, the D-region effectively disappears at night (*Nicolet and Aikin*, 1960). This significantly reduces the number of returned signals, and therefore this thesis uses radar data binned from $75km$ to avoid periods of low data availability. At regions above $90km$ several effects increasingly manifest themselves to make the radar winds less likely to be representative of the neutral winds.

3.2.2 Radiosonde

Radiosondes are small instrumentation packages carried aloft by balloons. They can measure a variety of atmospheric properties, generally temperature, pressure and humidity. As the balloon is generally not recovered, the data is transmitted back to the ground station for storage and later analysis.

The radiosonde can also provide wind velocity data if it is tracked by a ground-based radar or uses on-board GPS.

A global network of radiosondes are used to provide data for global climate models. These radiosondes are launched at 0000UTC and 1200UTC daily across the globe. The radiosondes used in this thesis are launched from McMurdo station, the data from these radiosondes is available online from 1994 to 2007[4].

[4]Archived Upper Air Data at http://amrc.ssec.wisc.edu/archiveraob.html

3.3 Governing equations

Following *Fritts and Alexander* (2003), *Andrews et al.* (1987) and *Read and Lewis* (2004) the equations describing gravity wave behaviour are given below. Equations 3.1 - 3.6 describe the unforced fundamental fluid equations relating to conservation of mass, momentum and energy.

$$\frac{Du}{Dt} - fv + \frac{1}{\rho}\frac{\partial p}{\partial x} = 0 \tag{3.1}$$

$$\frac{Dv}{Dt} + fu + \frac{1}{\rho}\frac{\partial p}{\partial y} = 0 \tag{3.2}$$

$$\frac{Dw}{Dt} + \frac{1}{\rho}\frac{\partial p}{\partial z} + g = 0 \tag{3.3}$$

$$\frac{1}{\rho}\frac{Dp}{Dt} + \frac{\partial u}{\partial x} + \frac{\partial v}{\partial y} + \frac{\partial w}{\partial z} = 0 \tag{3.4}$$

$$\frac{D\theta}{Dt} = Q \tag{3.5}$$

$$\theta = \frac{p}{\rho R}\left(\frac{p_0}{p}\right)^{\kappa} \tag{3.6}$$

The terms u, v, w give the fluid velocity vector in the horizontal and vertical directions; p is pressure; ρ is density; θ is potential temperature[5]; f is the Coriolis parameter due to the Earth's rotation (given by $f = 2\Omega sin\phi$, where Ω is the Earth's rotation rate and ϕ the latitude). Equation 3.6 represents the potential temperature,θ, the temperature a parcel of air would have if lowered adiabatically from p to p_0 (*Fritts and Alexander*, 2003); R is the ideal gas constant and $\kappa = c_p/c_\nu$ is the ratio of specific heat at constant pressure and volume.

Assuming a uniform horizontal hydrostatic state as per *Fritts and Alexander* (2003) with only horizontal wind, pressure and density varying only in the vertical dimension, equations 3.1 through 3.6 can be linearised to

$$\frac{Du'}{Dt} + w'\frac{\partial \bar{u}}{\partial z} - fv' + \frac{\partial}{\partial x}\left(\frac{p'}{\bar{\rho}}\right) = 0 \tag{3.7}$$

$$\frac{Dv'}{Dt} + w'\frac{\partial \bar{v}}{\partial z} + fu' + \frac{\partial}{\partial y}\left(\frac{p'}{\bar{\rho}}\right) = 0 \tag{3.8}$$

$$\frac{Dw'}{Dt} + \frac{\partial}{\partial z}\left(\frac{p'}{\bar{\rho}}\right) - \frac{1}{H}\left(\frac{p'}{\bar{\rho}}\right) + g\frac{\rho'}{\bar{\rho}} = 0 \tag{3.9}$$

$$\frac{D}{Dt}\left(\frac{\theta'}{\bar{\theta}}\right) + w'\frac{N^2}{g} = 0 \tag{3.10}$$

$$\frac{D}{Dt}\left(\frac{\rho'}{\bar{\rho}}\right) + \frac{\partial u'}{\partial x} + \frac{\partial v'}{\partial y} + \frac{\partial w'}{\partial z} - \frac{w'}{H} = 0 \tag{3.11}$$

[5]This is "the temperature a parcel of dry air at pressure p and temperature T would acquire if it were expanded or compressed adiabatically to the reference pressure $p_s = 1000mb$"(*Andrews et al.*, 1987)

$$\frac{\theta'}{\bar{\theta}} = \frac{1}{c_s^2}\left(\frac{p'}{\bar{\rho}}\right) - \frac{\rho'}{\bar{\rho}} \tag{3.12}$$

where the derivative

$$\frac{D}{Dt} = \frac{\partial}{\partial t} + \bar{u}\frac{\partial}{\partial x} + \bar{v}\frac{\partial}{\partial y} \tag{3.13}$$

is the linearised time derivative (*Fritts and Alexander*, 2003). All the primed quantities are perturbations to the background state. N is the Brunt-Väisälä (buoyancy frequency). Making the WKB approximation that the basic state varies slowly compared to the phase of the oscillations (i.e. the terms $\frac{\partial \bar{u}}{\partial z}$ and $\frac{\partial \bar{u}}{\partial z}$ in equations 3.7 and 3.8 are close to zero (*Gill*, 1982)), and assuming that the gravity wave solutions have the form

$$\left(u', v', w', \frac{\theta'}{\bar{\theta}}, \frac{p'}{\bar{\rho}}, \frac{\rho'}{\bar{\rho}}\right) = \left(\tilde{u}, \tilde{v}, \tilde{w}, \tilde{\theta}, \tilde{p}, \tilde{\rho}\right) \cdot \exp\left[i\left(kx + ly + mz - \omega t\right) + \frac{z}{2H}\right] \tag{3.14}$$

with k,l, and m as the x,y and z wavenumbers, then the differential equations simplify to a set of linear algebraic equations for monochromatic gravity waves. These are described by

$$-i\hat{\omega}\tilde{u} - f\tilde{v} + ik\tilde{p} = 0 \tag{3.15}$$

$$-i\hat{\omega}\tilde{v} - f\tilde{u} + il\tilde{p} = 0 \tag{3.16}$$

$$-i\hat{\omega}\tilde{w} + \left(im - \frac{1}{2H}\right)\tilde{p} + = -g\tilde{\rho} \tag{3.17}$$

$$-i\hat{\omega}\tilde{\theta} + \left(\frac{N^2}{g}\right)\tilde{w} = 0 \tag{3.18}$$

$$-i\hat{\omega}\tilde{\rho} + ik\tilde{u} + il\tilde{v} + \left(im - \frac{1}{2H}\right)\tilde{w} = 0 \tag{3.19}$$

$$\tilde{\theta} = \frac{\tilde{p}}{c_s^2} - \tilde{\rho} \tag{3.20}$$

where $\hat{\omega} = \omega - k\bar{u} - l\bar{v}$ is the intrinsic wave frequency (Lagrangian, i.e. relative to the background flow); H is the pressure scale height, equal to roughly $7km$ in the middle atmosphere; c_s the the speed of sound. Combining equations 3.15 through 3.20 into a single equation and demanding that the imaginary coefficients of the equation go to zero gives

$$\frac{g}{c_s^2} = \frac{1}{H} - \frac{N^2}{g} \tag{3.21}$$

$$\hat{\omega}^2\left(k^2+l^2+m^2+\frac{1}{4H^2}-\frac{(\hat{\omega}-f^2)}{c_s^2}\right) = N^2\left(k^2+l^2\right)+f^2\left(m^2+\frac{1}{4H^2}\right) \quad (3.22)$$

Equation 3.22 includes both acoustic and gravity waves. Letting $c_s \to \infty$ the gravity wave dispersion relation is calculated using

$$\hat{\omega}^2 = \frac{N^2\left(k^2+l^2\right)+f\left(m^2+\frac{1}{4H^2}\right)}{k^2+l^2+m^2+\frac{1}{4H^2}} \quad (3.23)$$

as given by *Fritts and Alexander* (2003).

To examine the properties of high frequency atmospheric waves, the Coriolis Parameter f is set to zero. As these waves are shorter than $1000km$ in horizontal wavelength means that they are relatively unaffected by the rotational effect of the Earth, thus the Coriolis term will be unimportant. In addition, a new horizontal wavenumber will be defined which combines x and y directions $k_h^2 = k^2 + l^2$

This gives the simplified dispersion relation as

$$\hat{\omega}^2 = \frac{N^2 k_h^2}{k_h^2+m^2+\frac{1}{4H^2}} \quad (3.24)$$

3.3.1 Gravity wave filtering

When a vertically propagating gravity wave encounters a region where the horizontal wind velocity matches its horizontal phase speed and direction of wave propagation, or the wind shear is too strong, it will be dissipated or reflected (*Fritts and Alexander*, 2003; *Whiteway and Duck*, 1996; *Makhlouf*, 1989). While the following is not a rigorous examination of gravity wave filtering, it should serve to broadly illustrate some of the associated phenomena.

3.3.1.1 Ducting (turning levels)

To examine ducting it will be assumed that the vertical wavelength is large compared to the horizontal wavelength.[6] In this case, the horizontal wavenumber will dominate the wave frequency which can then be described approximately by $\hat{\omega} = \hat{c_h} k_h$, where $\hat{c_h}$ is the intrinsic horizontal phase speed (the phase speed relative to the background horizontal flow). Substituting this into equation 3.24, the dispersion relation becomes

[6]Note that this assumption is only valid well away from critical levels as the vertical wavelength approaches zero in these regions. However, this assumption will nonetheless allow the derivation of simple equations showing the existence of a singularity at critical levels. Furthermore, it should also be noted that this assumption is only truly valid for very high intrinsic frequency waves.

$$(\hat{c_h}k_h)^2 = \frac{N^2k_h^2}{k_h^2 + m^2 + \frac{1}{4H^2}} \tag{3.25}$$

Rearranging this equation allows for an equation for the vertical wavenumber to be calculated

$$\begin{aligned} k_h^2 + m^2 + \frac{1}{4H^2} &= \frac{N^2k_h^2}{(\hat{c_h}k_h)^2} \\ m^2 &= \frac{N^2 - \hat{c_h}^2\left(k_h^2 + \frac{1}{4H^2}\right)}{\hat{c_h}^2} \end{aligned} \tag{3.26}$$

When m is positive the wave is propagating downward; when negative, it propagates upward. However, if m becomes imaginary, the wave will become evanescent, which will be of importance below.

Equation 3.25 can be solved for the horizontal wavenumber in a similar fashion giving the following equation

$$k_h^2 = \frac{N^2 - \hat{c_h}^2\left(m^2 + \frac{1}{4H^2}\right)}{\hat{c_h}^2} \tag{3.27}$$

Note that when k is positive the wave will be propagating in the positive horizontal direction. Examination of equation 3.26, shows that if the term $\hat{c_h}^2\left(k^2 + \frac{1}{4H^2}\right)$ is larger than N^2, then m^2 will be less than zero. When m^2 is negative the wave is evanescent, and as such the wave will experience total reflection at the point where $m^2 = 0$. So for vertical propagation the following condition must be met.

$$\hat{c_h}\left(k^2 + \frac{1}{4H^2}\right) > N^2 \tag{3.28}$$

If a mountain wave is considered, the horizontal phase speed c_h is zero. The intrinsic phase speed given by

$$\hat{c_h} = c_h - u_h \tag{3.29}$$

where c_h is the doppler-shifted phase speed and u_h is the background horizontal wind becomes

$$\hat{c_h} = -u_h \tag{3.30}$$

Substituting into equation 3.28 and solving for u_h^2 gives

$$u_h^2 < \frac{N^2}{k_h^2 + \frac{1}{4H^2}} \tag{3.31}$$

in order for the wave to propagate upward. A wave propagating to higher levels cannot pass through regions where the horizontal wind shear is too strong. In addition, large horizontal wavenumbers (short wavelengths) are more likely to be reflected, since the maximum wind shear is lower. This is similar to total internal reflection in optics – indeed, if there is a discontinuity in N, partial reflections can occur (*Gill*, 1982). The approach to a turning level takes a finite amount of time, and as such many of the dissipative effects discussed below do not have sufficient time to act on the wave.

3.3.1.2 Critical level filtering

Equation 3.26 indicates that a gravity wave will have an infinite wavenumber whenever the intrinsic phase speed ($\hat{c_h}$) is zero. In the Eulerian frame, the wave cannot exist whenever the Doppler-shifted horizontal phase speed equals the horizontal background wind velocity.

A vertically propagating gravity wave will never actually reach a critical level. This is shown by examination of equations 3.27 and 3.26; as the intrinsic phase speed ($\hat{c_h}$) approaches zero, m^2 approaches infinity (providing k_h^2 is small and m^2 remains positive). Since the vertical wavelength is the inverse of m, it will approach zero as the wave approaches the critical level. In addition, the energy transported vertically by the wave moves at the vertical group velocity $v_g = \frac{\partial \omega}{\partial m}$. Differentiating equation 3.24, with respect to vertical wavenumber, gives

$$v_g = \frac{2k_h^2 m N^2}{\left(k_h^2 + m^2 + \frac{1}{4H^2}\right)^2} \tag{3.32}$$

$$\lim_{m \to \infty} v_g = 0 \tag{3.33}$$

Equation 3.33 indicates that energy cannot pass through a critical level. This, combined with the vertical wavelength going to zero, qualitatively shows that the wave will asymptotically approach the critical level. Since energy travelling at the vertical group velocity of the wave would take an infinite amount of time to reach a critical level, processes which are normally unable to act on the wave have time to do so (*Gill*, 1982; *Salby*, 1996). Because the wave frequency is zero at the critical level, wave activity is frozen relative to the background flow (*Salby*, 1996, ch 14.3). This allows processes which would not usually have time to have a significant effect on the wave propagation to have a strong effect; the wave loses energy through Newtonian Cooling as some of its energy is radiated into space as heat. This process is particularly significant during the polar winter.[7] The wave also loses energy through viscous damping, which increases as the wave approaches the critical level and decreases in scale (*Gill*, 1982). Note that these effects can still cause significant dissipation of the wave

[7]Newtonian cooling is also responsible for radiative relaxation, an effect which can be apparent in lower frequency gravity waves(*Andrews et al.*, 1987)

in the absence of a critical level provided that the background flow speed gets close enough to the phase speed.

3.3.2 Blocking Circles

One way to examine critical levels is by using blocking circles, which are defined in (*Taylor et al.*, 1993). These are given by:

$$\Omega = \omega\left(1 - \frac{U\cos\phi + V\sin\phi}{\nu_x}\right) \tag{3.34}$$

where Ω is the Doppler-shifted velocity of a given gravity wave. U and V are the zonal and meridional background wind components respectively, ϕ indicates the horizontal direction of wave propagation, and ν_x its phase speed. Based on background flow given by U and V, a gravity wave with properties ω , ϕ and ν_x will be considered blocked if Ω is less than zero (*Taylor et al.*, 1993). Graphically, this gives a circle with a radius of $\sqrt{U^2+V^2}$ centred on the Cartesian coordinates (U, V) (see Figure 6.1). If a gravity wave's horizontal propagation direction and phase speed are within this circle, it will be unable to propagate any higher. Thus, these circles identify portions of the parameter space through which waves cannot propagate to higher altitudes.

This is a powerful technique, as it allows an easy representation and quantification of gravity wave critical level filtering. For this reason, the concept of blocking circles shall be expanded on in Chapter 6 to develop an atmospheric transfer function for the atmosphere above Scott Base using model data.

3.3.3 Effects of gravity waves in the atmosphere

One of the more significant effects of gravity waves in the atmosphere is observed in the high-latitude mesosphere. During the winter months, when this region is predominantly in the dark, it is actually warmer than during the summer months when it experiences almost 24-hour sunlight. This seemingly counter-intuitive fact is due to the effects of gravity waves.

Gravity waves propagating upward from their sources (generally in the troposphere) grow exponentially with height. This is due to the exponential decrease in atmospheric density; as these wave amplitudes grow larger, they become unstable and begin to break as illustrated in Figure 3.5. While the actual mechanics of gravity wave breaking are quite complex (*Isler et al.*, 1994; *Fritts et al.*, 1994; *Andreassen et al.*, 1994) a simplified explanation will serve for the descriptive use of gravity wave breaking in this thesis.

As the wave amplitude grows, it reaches a point where it becomes unstable. For gravity waves with high intrinsic frequency, the usual breaking mechanism is convective instability (*Fritts and Alexander*, 2003). Once the wave has begun to break, its growth is halted as it transfers energy (in the form of turbulence) to the background medium. The breaking wave attempts to drag the background flow towards its own phase speed. This gravity wave drag transfers momentum from the lower atmosphere to the altitude range over which the wave is

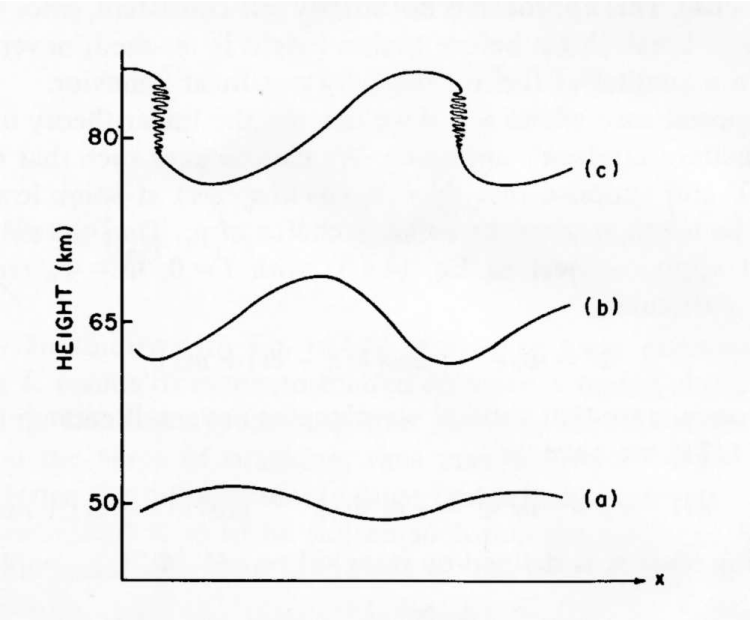

Figure 3.5: Simple model of breaking wave breaking from (*Andrews et al.*, 1987).

breaking. *Lindzen* (1981) noted that the acceleration as a result of these breaking waves was more than sufficient to account for the mesosphere's winter warming and summer cooling.

The process of summer cooling and winter warming works as follows; during the summer, the westward stratospheric jet causes westward-propagating waves to experience critical level filtering. However, eastward propagating waves will reach the mesopause where, as their amplitudes grow, they begin to break, transferring momentum to the background flow. This creates a eastward (or prograde) jet in the mesosphere, as well as a general eastward "body force" in the atmosphere in the region of breaking (*Lindzen*, 1981; *Holton and Alexander*, 2000; *Garcia and Boville*, 1994). Because the jet is moving in the prograde direction, it has excess angular momentum. To balance this, the air is forced away from the pole while conservation of mass requires it to be replaced by air from below. In the winter hemisphere the opposite effect occurs; the eastward stratospheric jet filters out eastward propagating waves, enabling westward waves to break in the mesosphere. This produces a westward jet with insufficient angular momentum, and therefore air moves toward the pole where it displaces air downward. This results in a pole-to-pole circulation.

The vertical motion of air in the summer hemisphere results in adiabatic cooling as the air parcel is expanded. This results in the cold summer mesosphere while the downward motion of air near the winter pole results in adiabatic compression and hence heating.

3.4 Conclusion

Having introduced gravity waves and some of their associated phenomena, the following two chapters will develop gravity climatologies above Scott Base both in the lower atmosphere and the MLT using radiosondes and the Scott Base MF-radar respectively.

Chapter 4

MLT Gravity Wave Climatology

4.1 Introduction

This chapter develops a climatology of gravity waves in the Mesosphere Lower Thermosphere (MLT) using the Scott Base MF-radar data described in the previous chapter. Gravity waves propagating up from the lower atmosphere are acted upon by the wind field on their way to the MLT. These background winds can result in critical level filtering when their velocity vector matches the horizontal phase speed and propagation direction of the gravity waves. The filtering effects can be modelled by an atmospheric transfer function. The observed MLT gravity wave climatology can be used to examine the parameters required to derive a realistic atmospheric transfer function.

The climatology is produced using the Scott Base MF-radar measurements of the zonal and meridional winds between 70 and 96km. The wind data is composed of several signals; these include the mean wind speed and perturbations associated with long period atmospheric waves, such as the diurnal and semi-diurnal waves, as well as atmospheric gravity waves. Removing all long period waves and long term trends from the wind data leaves only the wind perturbations associated with gravity waves and some instrumental noise.

Assuming that the noise is small, the kinetic energy per unit mass is calculated using the zonal and meridional wind perturbations. This energy is used as the gravity wave climatology for the year. Averaging several years together produces the overall gravity wave climatology.

4.2 Methodology

The techniques used to process the MF-radar data and develop a gravity wave climatology are common in the literature (see *Vincent and Fritts*, 1987; *Dowdy et al.*, 2007). This thesis models its method on that found in *Hibbins et al.* (2007). However, it should be noted that while the *Hibbins et al.* (2007) study bins the radar data at two-minute resolutions, this was not done in this study in order to reduce the computational overhead of the method.

Initially, the radar data was placed into 26 bins from 70 - 96km, the data region dictated by the radar data acquisition and high signal-to-noise ratio. All winds greater than

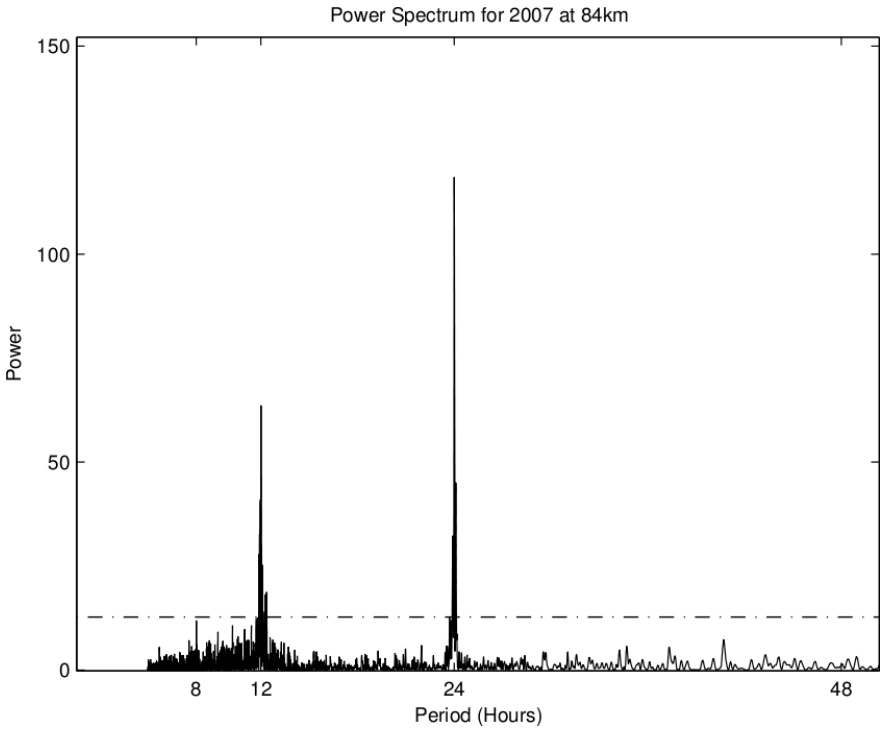

Figure 4.1: The wave periods present in the radar wind data in 2007. The dashed line is the 99% significance level.

$100ms^{-1}$ were discarded at this point in order to remove the occasional artificially large wind measurement due to errors in the FCA algorithm. (Chapter 3.2.1). Note that while there is some radar wind data below $70km$, the very weak D-region during the polar night means that the data availability is too low to be of use. The last height bin was selected to be $96km$; above this altitude, ionisation becomes increasingly strong and electromagnetic effects become important (*Fraser*, 1984b). These electromagnetic effects mean that the assumption that the diffraction pattern observed by the radar moves due to the neural wind is likely to be violated. Furthermore, as height increases above 90km, very strong reflections from the E-region of the ionosphere can contaminate winds measurements, producing false winds (*Hocking*, 1997; *Namboothiri et al.*, 1993)

Long period waves, such as the diurnal, semidiurnal and terdiurnal waves, often dominate the velocity field and therefore need to be removed to obtain wind perturbations from gravity waves alone. This was done by least square fitting a set of known period waves to the data and then removing them from each height bin. The periods of the waves to be fit were determined using a Lomb-Scargle periodogram (Figure 4.1). This gave strong peaks at 12 and $24h$, and a weaker peak at $8h$. These periods correspond to the diurnal, semi-diurnal and terdiurnal waves which would be expected to be present in this region.

Because the strength of the long period waves vary over time, the least squares fitting was performed over a five-day sliding window, applied to hourly average winds in order to reduce the effect of noise and speed up the computation. If the hourly mean was comprised of fewer than four data points, it was discarded. If less than 24 data points made up the data for the five-day sliding window (20% of the maximum possible data), then there were also considered to be too few data points for reliable removal of the long period waves. As such,

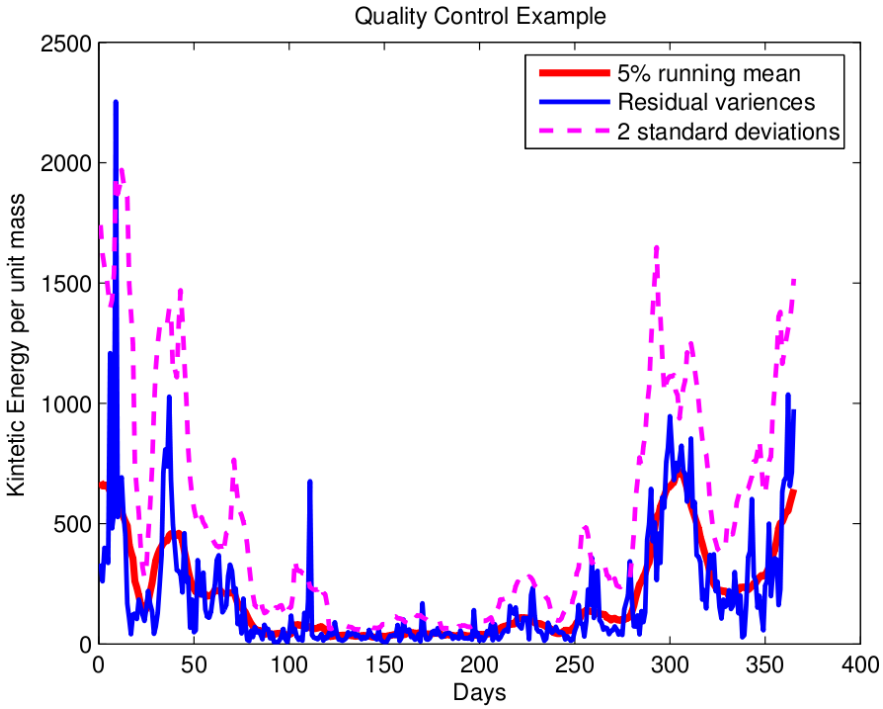

Figure 4.2: Example of radar gravity wave energy quality control

the day in the centre of a given five-day sliding window was not considered in the analysis. The equation used in the least squares fitting routine used in this analysis to remove the long period waves is shown below

$$\begin{aligned} y &= A\cos(-\omega_{24}t) + B\sin(-\omega_{24}t) + C\cos(-\omega_{12}t) + D\sin(-\omega_{12}t) \\ &\quad + E\cos(-\omega_{8}t) + F\sin(-\omega_{8}t) + Gt + H) \end{aligned} \tag{4.1}$$

where $\omega_{24}, \omega_{12}, \omega_8$ are the frequencies of the diurnal wave, semi-diurnal and terdiurnal waves respectively; Gt and H are the linear trend and DC offset; $A - H$ are the least squares fit parameters. For example $A\cos(-\omega_{24}t) + B\sin(-\omega_{24}t)$ makes up the diurnal wave.

Each five day window the waveform of the long period waves was reconstructed from the least squares fit parameters and then subtracted from the radar data. The variance of the residual was then taken giving u'^2 and v'^2. It was assumed that this variance was due to gravity waves and some noise component. An additional quality control step was performed at this point to ensure that there were at least three data points in each least squares fitting set (per hour), and that they were less than two standard deviations away from a 15-day sliding mean over of the variance. Assuming a lognormal distribution, the variances were then reduced to daily means, which served to mitigate the effect of any white noise present.

The kinetic energy per unit mass is given by:

$$Ek_m = \frac{1}{2}(u'^2 + v'^2) \tag{4.2}$$

Taking the mean of the Ek_m across a set of years yielded the gravity wave climatology for those years.

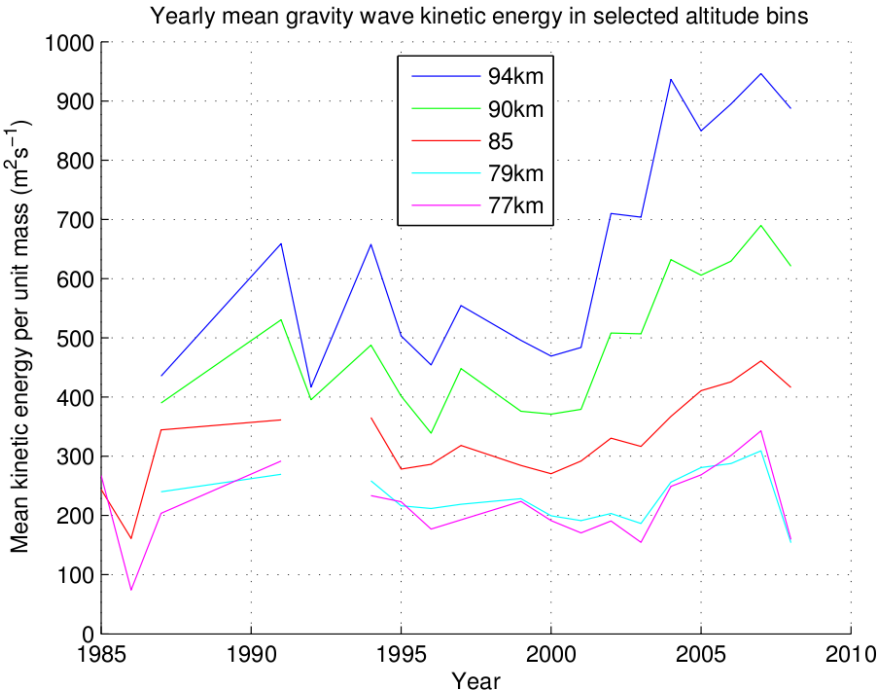

Figure 4.3: Averaging the gravity wave kinetic energy for each height bin and year.

It was particularly important to consider the quality of the MF-radar data, as the MF-radar had undergone a substantial upgrade early in 2004. The upgrade involved a change to the radar control and data acquisition (*Baumgaertner et al.*, 2006). This resulted in a significantly higher rate of data acquisition: in early 2004, the usual time between sampling periods was around eight minutes, while in early 2005 the system was collecting data at one set per minute. To test the effect of the upgrade, the gravity wave field was calculated for each year from 1985 to 2008, averaged across the whole year for each height bin taken. Figure 4.3 shows that after 2005 there was a large increase in the mean kinetic energy per unit mass, particularly at higher altitudes. For this reason, the final gravity wave climatology was generated using only data from 2005 to 2008.

In order to ensure that the climatology produced over such a short timespan was representative, an additional climatology was produced for the period from 1985 to 2004. While the magnitudes of gravity wave structures could be expected to differ because of the radar data acquisition upgrade, a broad similarity in the structures themselves would add credence to the 2005 to 2008 climatology.

Lastly, the data between 2005 and 2008 was checked for any obvious anomalies that were not removed by the usual quality control methods. This was done by calculating the gravity wave climatology and checking each height bin for variations between years. Figure 4.4 shows an anomalous section of data in 2006 from the 4^{th} of June to the 29^{th} of July. As this anomaly was present at all altitudes, it was manually removed.

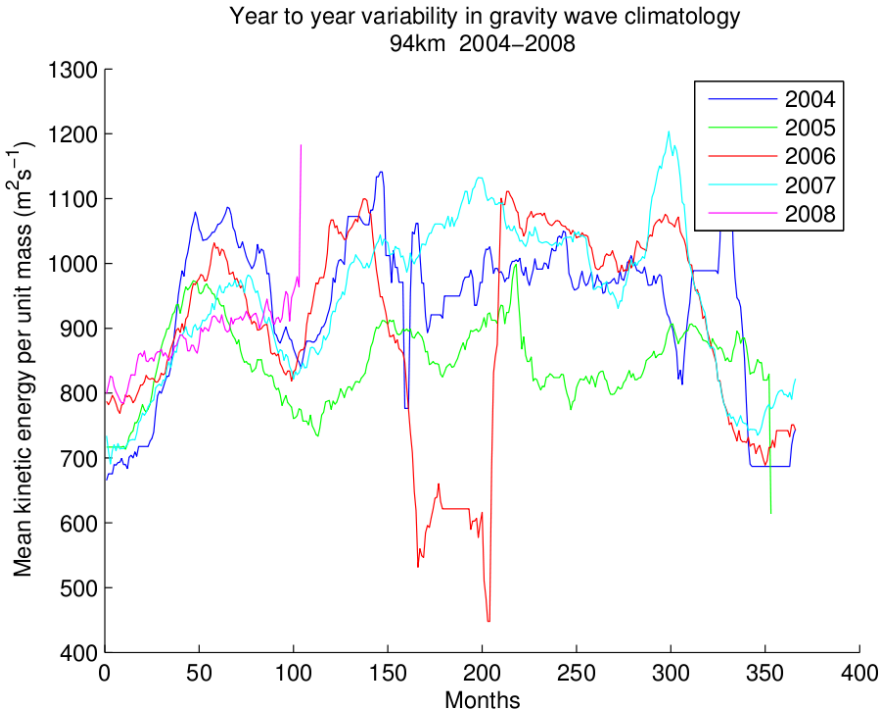

Figure 4.4: An early analysis of the variations in gravity wave energy between the years of the climatology revealed and anomalous section of data in 2006.

4.3 Results and discussion

The gravity wave climatology produced using MF-radar data between 2005 and 2008 is shown in Figure 4.5. It shows a general increase in gravity wave energy with height, due to gravity waves growing as the atmospheric density drops. The gravity wave field also shows strong seasonal patterns: during the Southern Hemisphere summer months there is generally less gravity wave activity than during the rest of the year. This is particularly apparent at altitudes below 85km where the gravity wave kinetic energy per unit mass is particularly weak around the equinoxes.

Since producing a climatology spanning a little over three years is potentially statistically unreliable, a climatology spanning 1985 to 2004 was also produced. While the magnitude of the pre-2005 climatology (Figure 4.6) is lower than the post-2005 climatology (particularly at higher altitudes), its overall structure is similar to that shown in Figure 4.5. This structural similarity increases confidence that the 2005-2008 climatology is not composed of a set of anomalous years, and that the radar accurately observes gravity wave fields.

Beginning in April and lasting through the winter, there is a relatively high degree of gravity wave energy at low altitudes. The gravity wave energy per unit mass decreases with altitude for approximately 4km before beginning to increase. It is possible that this feature is an artifact resulting from the weak polar night D-region producing too few data points for meaningful fits. However, even dramatically increasing the quality control thresholds such that significant amounts of data were rejected does not affect the persistence of this feature.

Another theory is that this winter feature is due to tropospheric/low stratospheric gravity waves propagating into the mesosphere, as these waves have been shown to be stronger in the Antarctic winter and spring(*Yoshiki et al.*, 2004). This would correspond with the weaker

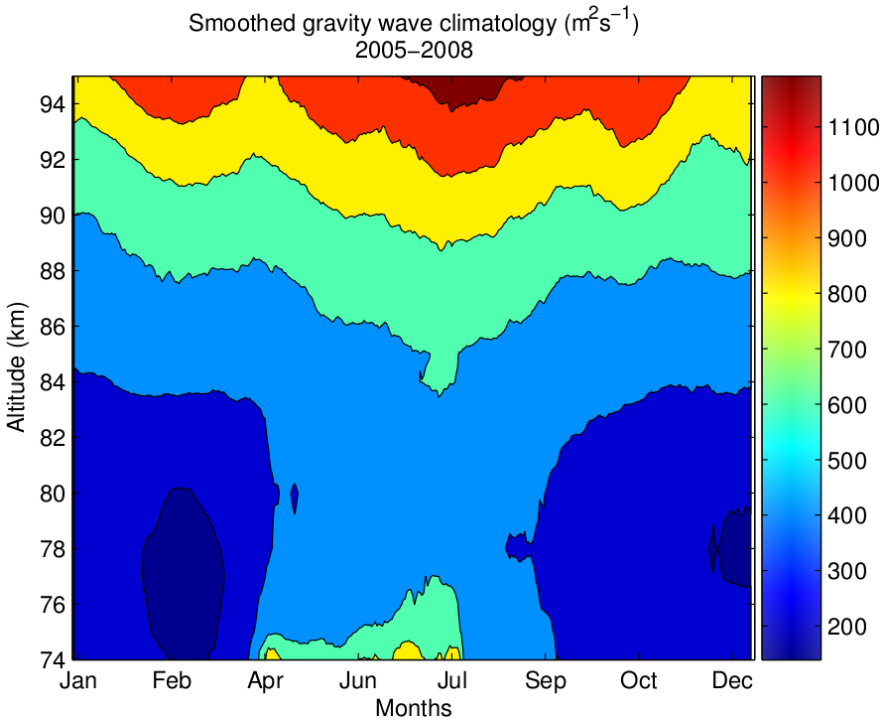

Figure 4.5: Gravity wave climatology derived from the Scott Base MF-radar over 2005 to early 2008. Derived from variances of the wind residuals after removing tidal components. Smoothed with a 10% sliding window.

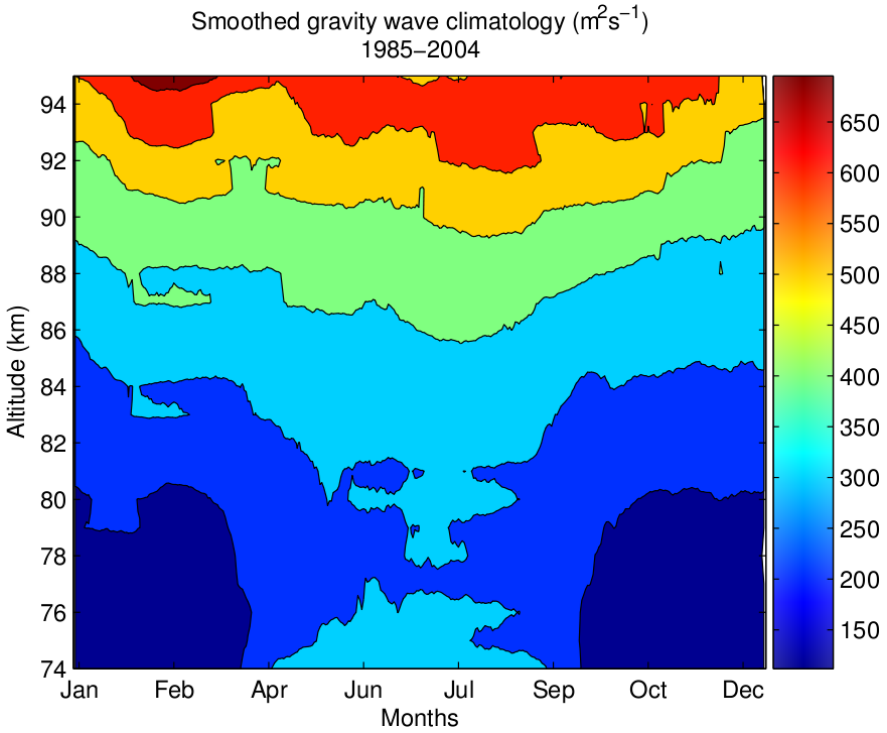

Figure 4.6: Gravity Wave climatology 1985-2003, prior to the upgrade of the data acquisition system of the Scott Base MF-radar. Smoothed with a 10% sliding window.

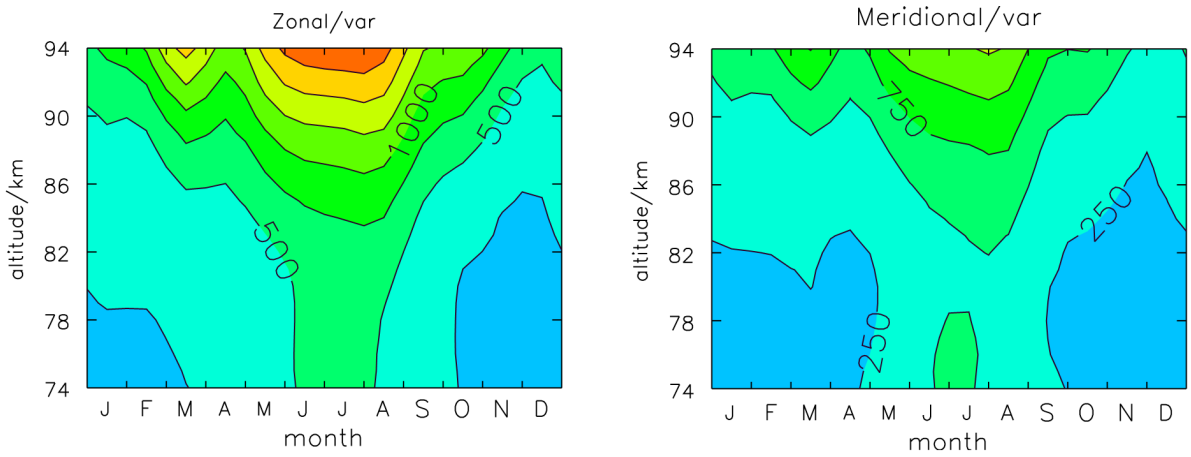

Figure 4.7: Climatology of monthly mean wind variances between 1997 and 2005 at Rothera, from *Hibbins et al.* (2007). These wind variances are taken to be associated with gravity wave activity.

summer gravity wave energy observed in this region. The lower gravity wave energy in the summer mesosphere could also be due to gravity wave filtering by the atmospheric transfer function, preventing the gravity waves from reaching the region examined by the MF-radar.

The rapid increase in gravity wave energy observable at 74-76km in Figure 4.5 could also be due to the formation of the polar night jet at this time of year. This has been shown to generate gravity waves, possibly as a result of geostrophic adjustment around the jet (*Sato*, 2000; *Sato et al.*, 1999).

The overall pattern observed at Scott Base is similar to gravity wave climatologies produced at other stations in Antarctica. A selection of climatologies by *Dowdy et al.* (2007) and *Hibbins et al.* (2007) are given in Figures 4.7 and 4.8 for comparison. Both of these climatologies display similar features to those of the Scott Base climatology in Figure 4.5, increasing confidence in the reliability of its overall structure despite the short time period.

Figure 4.9 compares the gravity wave energy for each year in the 2005 - 2008 as well as the 1985 - 2004 data. It suggests a large inter-annual variability in the magnitude of the gravity wave energy, as well as some variability in the overall distribution of waves throughout the year. However, the overall structure of the gravity wave kinetic energies in Figures 4.5 and 4.6 are similar. This, along with the the similarities to gravity wave energy climatologies at other locations in Antarctica, suggests that the overall climatology may be sufficiently indicative of conditions to provide a meaningful comparison of the impact of the atmospheric transfer function on gravity waves from the lower atmosphere. Nonetheless, an ideal fitting should be done to a single subjectivly good year of MF-gravity wave data and radiosonde data as a test. Unfortunately, good radiosonde years and good radar years do not overlap. With more data in the future, this may not be the case and this test could be performed.

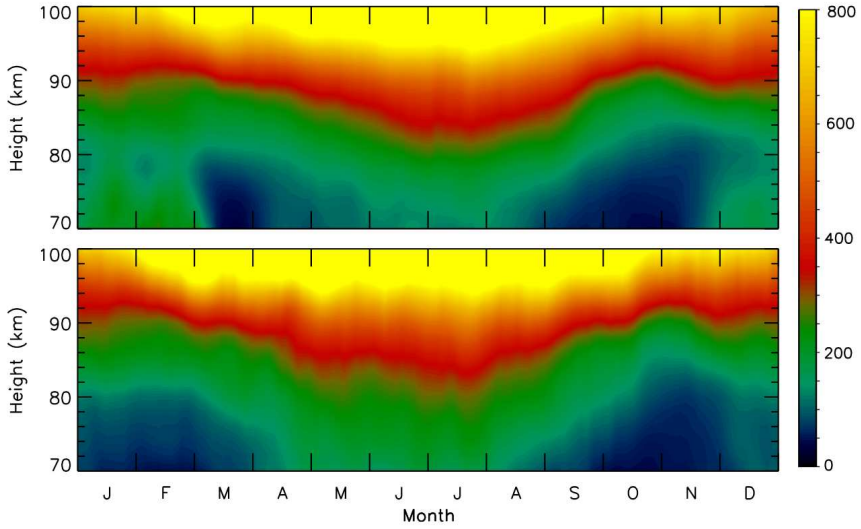

Figure 4.8: Climatology of zonal and meridional wind variances after removal of tidal components at Davis (top panel) and Syowa (bottom panel). Adapted from *Dowdy et al.* (2007).

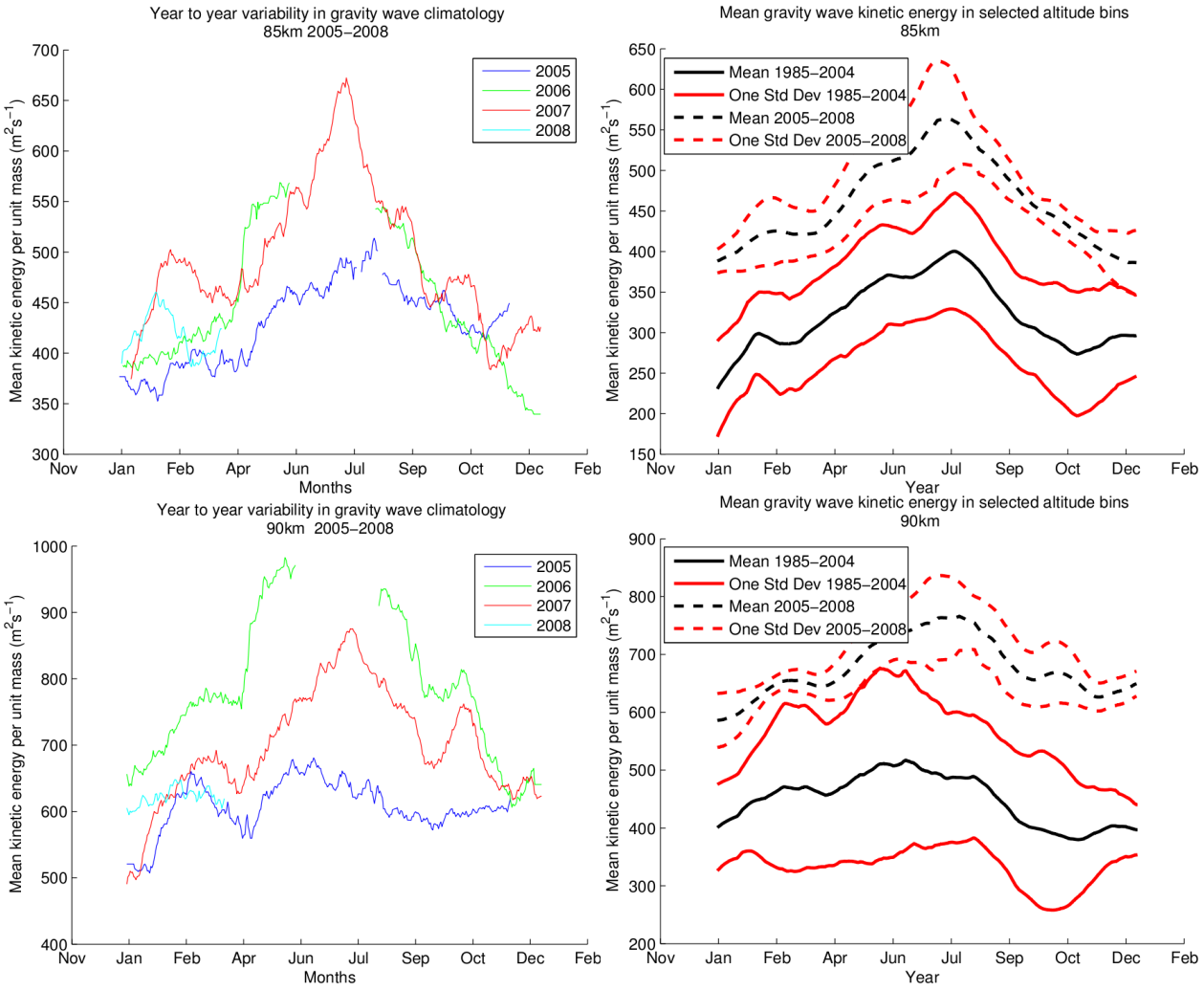

Figure 4.9: Variability of gravity wave kinetic energy between years and before and after data acquisition upgrade.

Chapter 5

Radiosonde Derived Gravity Wave Source Function

5.1 Introduction

Gravity waves propagating from the lower atmosphere are modified by various processes, such as critical level filtering and gravity wave breaking. The integrated effect of these processes can be modelled by an atmospheric transfer function. This transfer function can be multiplied by a source function – a measure of the wave activity variation associated with sources alone – to produce a simulation of the high altitude gravity wave field discussed in the previous chapter. This chapter seeks to determine an empirical source function for gravity waves based on radiosonde observations from balloons launched from McMurdo Base, Antarctica.

Using established techniques, the kinetic and potential energy associated with gravity waves were calculated at a variety of altitudes over the period from 2000-2007. The sum of the potential and kinetic energy is referred to as the total gravity wave field. The gravity wave source function is calculated over a variety of altitudes in the troposphere and over the tropopause/lower stratosphere. Analysing the interaction of the source functions with the atmospheric transfer function should provide insight into the contribution of low altitude gravity wave variability to the high altitude (75-96km) wave field. For example, if the filtered source function displays a low correlation to the observed gravity wave climatology, this could indicate that waves were being generated at higher altitudes, or that gravity waves were moving horizontally into the observation area. Finally, crude gravity wave phase direction information can be obtained by fitting ellipses to hodographs of wind changes with altitude.

5.2 Methodology

Gravity waves in the troposphere can be produced in several ways (see Section 3.1.1). The primary mechanisms are: flow over mountains, shear generation, geostrophic adjustment

and deep convection (*Fritts and Alexander*, 2003). Since the Antarctic is too cold for any significant convective activity, the last source can be omitted from this discussion.

The gravity wave source function was calculated using data from radiosondes launched at McMurdo Station, which is approximately 1.5km south of the receiving antennas at Arrival Heights. It can therefore be assumed that these radiosonde observations are indicative of atmospheric conditions similar to the Arrival Heights MF-radar, though obviously they examine different altitude ranges.

The source functions are defined by the gravity wave field in the troposphere and in the stratopause. The gravity wave field is obtained from wind velocity vectors and temperature measurements sampled by radiosondes as they rise through the air column. Calculations of gravity wave activity measures are completed using well-established methods discussed in *Vincent and Alexander* (2000) and *Tsuda et al.* (2004). Briefly, the radiosonde data is placed into altitude bins in order to be consistent between successive flights. After binning the data, a second order polynomial is fitted to the temperature profile and wind speeds in the zonal and meridional directions. This polynomial is subtracted from the raw data in order to obtain the gravity wave perturbations around the mean.

The gravity wave field is then given by the sum of the kinetic and potential energy per unit mass at each altitude bin. The relevant equations are

$$E_k = \frac{1}{2}\left(u'^2 + v'^2\right) \tag{5.1}$$

where E_k is the kinetic energy per unit mass, and u' and v' are the zonal and meridional components of the perturbation velocities. Note that the vertical component of the kinetic energy is ignored, as it is considered too small to be of significance (*Yoshiki and Sato*, 2000).

The potential energy per unit mass(E_p) is calculated using

$$E_p = \frac{1}{2}\left(\frac{g}{N}\right)^2\left(\frac{T'}{T_0}\right) \tag{5.2}$$

where T' is the temperature perturbation; T_0 is the mean temperature profile as measured by the radiosonde; g is gravitational acceleration, and N is the Brunt-Väisälä frequency, which (following *Andrews et al.* (1987)) is given by:

$$N^2 = g\left(\frac{T}{T_s}\right)\frac{\partial \ln\theta}{\partial z} = \frac{R}{H}\left(\frac{\partial T}{\partial z} + \frac{\kappa T}{H}\right) \tag{5.3}$$

The terms T and T_s are the temperature with respect to altitude and surface temperature respectively; g is the acceleration due to gravity; R is the gas constant for air; θ is the potential temperature; H is the scale height, which varies from $6km$ in the troposphere to roughly $7km$ in the stratosphere; $\kappa \equiv R/c_p \approx 2/7$ where c_p is the specific heat at constant pressure.

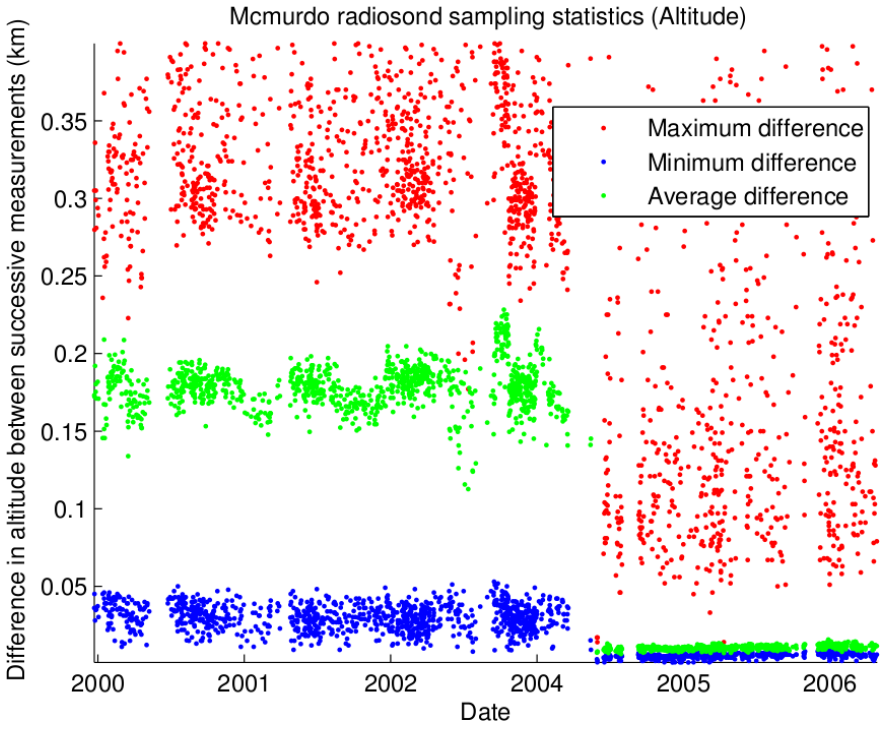

Figure 5.1: McMurdo radiosonde sampling altitude statistics between 1 and $8km$. Each balloon flight between 2000 and the start of 2007 is displayed. The average difference in altitude between measurements is displayed, as well as the maximum and minimum difference for each flight.

The kinetic and potential energy are calculated for each radiosonde flight. The energies are then converted to daily averages assuming a lognormal distribution.

Ideally to obtain gravity wave data, high vertical resolution data should be used (*Vincent and Alexander*, 2000). *Tsuda et al.* (2004) use $100m$ vertical resolution data, while *Vincent and Alexander* (2000) and *Yoshiki and Sato* (2000) use 50m binning. In order to determine the altitudes for the McMurdo radiosonde data, the average difference between successive altitudes in the raw data $\left(\overline{\Delta z}\right)$ is plotted for each flight in the measurement period between 2000 and 2007. Figures 5.1 and 5.2 show that the quality of data available varies quite substantially before and after mid-September 2004. The value of $\overline{\Delta z}$ prior to this date is roughly $175m$, while afterward the average difference is less than $15m$.

The large difference between $\overline{\Delta z}$ and the the maximum and minimum differences prior to September 2004 suggests that there may be some relationship between sampling altitude (z) and the height difference (Δz) between measurements. This possibility is examined in Figure 5.2: linear fitting Δz compared to z yields a slope for each radiosonde launch. A slope of zero indicates that the sampling is taking place at a regular interval throughout the entire radiosonde flight, while a positive slope indicates that the sampling takes places at ever increasing Δz throughout the flight. The figure shows that prior to 2005 the height difference between measurements increased with altitude. In addition, the the rate at which the height differences increased with height varied substantially between radiosonde launches. Prior to the program upgrade, Δz increases by roughly $1.5m$ every $100m$. After the upgrade Δz is effectively constant with increasing altitude.

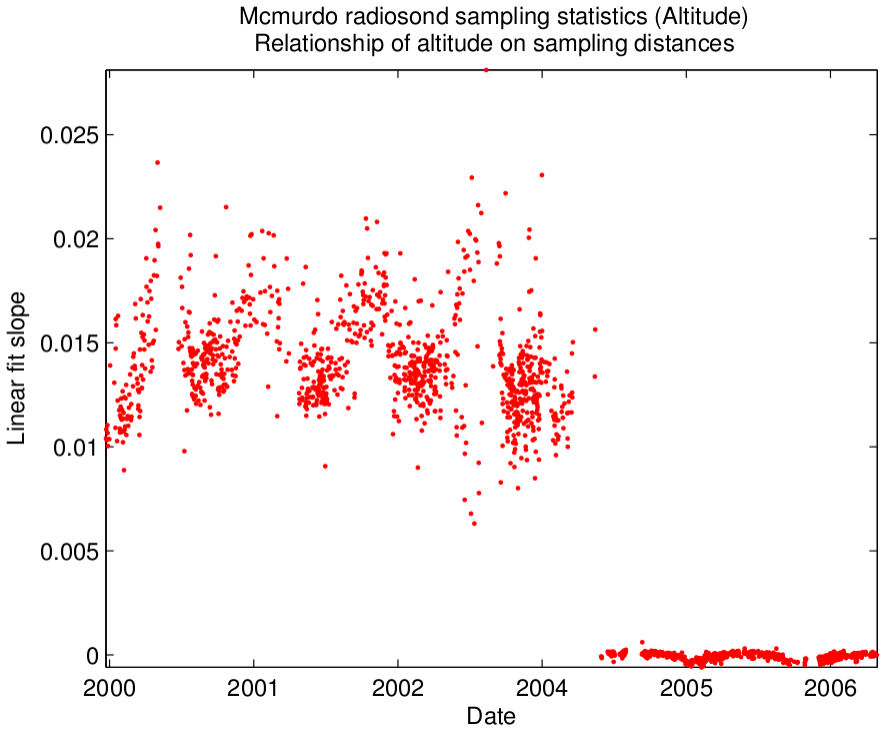

Figure 5.2: Another way of examining the radiosonde's data sampling is to calculate the least squares linear slope of differences in height vs. sample number.

While the increase of Δz with height prior to the upgrade is fairly small, the fairly coarse vertical scale will remove part of the gravity wave spectrum. Ideally, this would mean that only data after 2005 should be used. However, the McMurdo radiosonde data is currently unavailable after 31st of March 2007, which leaves only two years of data. This may be insufficient to be representative, particularly in light of the likely variations in the gravity wave field over several years. Therefore, data from 2000 to 2007 is used and binned every $200m$, as this is the average distance between height measurements for the pre-2005 McMurdo radiosonde data (see Figure 5.1).

Binning the radiosonde data every $200m$ introduces an observational filter to this data, removing small vertical wavelength gravity waves (*Alexander*, 1998). For this reason, complementary source functions are produced with a $40m$ binning. However, these will only be produced after September 2004, when the data quality becomes sufficient to justify this resolution. The data binned at $200m$ will be used to verify that the climatology produced with $40m$ altitude resolution is reasonable.

Climatologies are produced over two altitude ranges:

- from $1-8km$ (within the troposphere), the region in which gravity waves, particularly topographic gravity waves, are generated;
- from $9-13km$, the region which generally encompasses the tropopause. It should be noted that the height of the tropopause varies substantially through the Antarctic year and is very poorly defined in winter (*Zangl and Hoinka*, 2001). This region is of interest, as gravity waves generated by geostrophic adjustment processes around the polar night jet can be observed here (*Sato*, 2000).

Finally, in order to obtain some information about wave propagation directions, hodographs were produced for each radiosonde flight. Hodographs trace out the perturbation wind vector with height (see Figure 5.6). The hodographs form ellipses; the major axis of the ellipse indicates the horizontal propagation direction of the wave (albeit with a 180 degree ambiguity) (*Vincent and Alexander*, 2000).

5.3 Results

The average kinetic energy through $1 - 8km$ and $9 - 13km$ and across the period from $2000 - 2007$ using $200m$ and $40m$ binning is shown in Figure 5.3. These figures also show the average kinetic energy over the height range using data acquired after the McMurdo radiosonde both before and after the radiosonde upgrade. A notable feature in the $40m$ binning case (post-upgrade) is a strong springtime increase in kinetic energy, which is absent in the $200m$ case.

In order to examine the possibility that the two years after the program upgrade might be atypical, the kinetic energy per unit mass was plotted for each year and each altitude bin. Figure 5.4 shows two sample altitude bins, 4 - $5km$ and 12 - $13km$. The figure shows that the years after the radiosonde programme upgrade are not obviously anomalous within the mean and standard deviation.

This means that the absence of the spring time warming in the pre-upgrade filtering could be attributed to observational filtering (see *Baumgaertner and McDonald*, 2007; *Alexander*, 1998), though this difference may be due to interannual variability in the source function. The springtime increase in gravity wave kinetic energy has been noted in several studies, such as *Yoshiki and Sato* (2000) and *Baumgaertner and McDonald* (2007). *Yoshiki and Sato* (2000) show that this springtime gravity wave enhancement occurs in regions of high static stability, and may be related to a shift in the polar vortex both increasing static stability as well as gravity waves being generated by the vortex itself. The lack of such a ubiquitous feature in the $200m$ binning data means that the $40m$ resolution data will also have to be considered when examining the effect of the atmospheric source function of these low altitude waves, even though there is little more than two years of data.

A notable feature in the gravity wave climatology near the tropopause level (shown in Figure 5.3) is the rapid increase in gravity wave energy starting in April. This corresponds to the onset and strengthening of the polar night jet (see Figure 2.5). This phenomenon has been mentioned in several papers including *Whiteway et al.* (1997).

A similar structure is observed in the gravity wave potential energy (see Figure 5.5). This adds some credence to the gravity wave kinetic energy per unit mass climatology as the ratio of kinetic energy to potential energy is theoretically relatively constant as indicated in *Ratnam et al.* (2004); *Nastrom et al.* (2000). Note that the finer details vary between the E_k and E_p cases, this leaves room for possible improvement by including the potential energy in the gravity waves source function calculation.

Lastly, an attempt was made to determine the variability in wave propagation directions through the use of hodographs. An example hodograph for the 23^{rd} of September 2005 is shown in the right panel of Figure 5.6. The major axis of the ellipse indicates the propagation

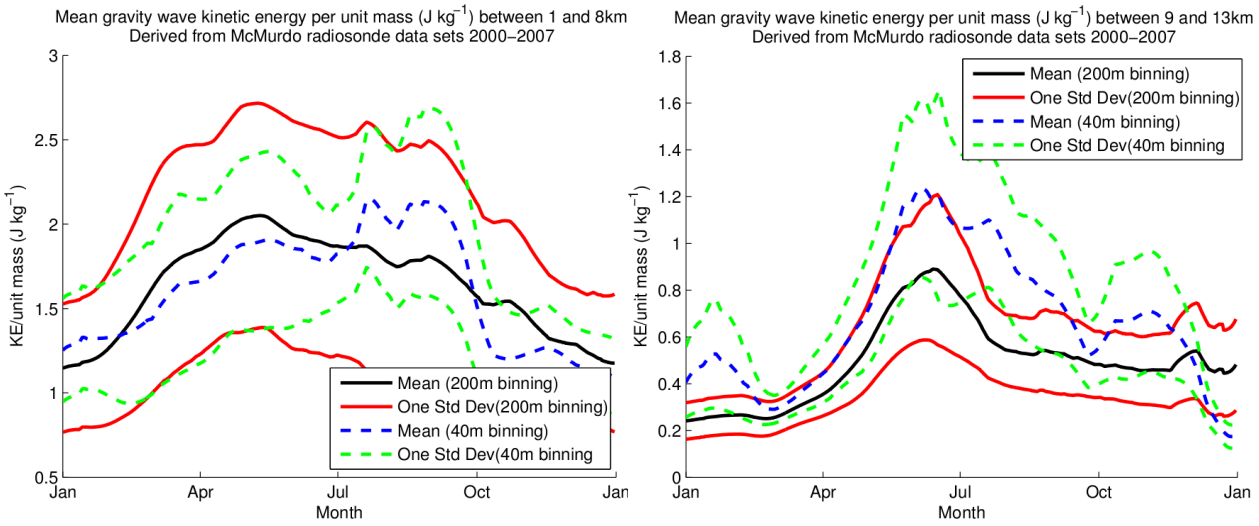

Figure 5.3: The total mean gravity wave kinetic energy between $1-8km$ and $9-13km$ at 200m vertical resolution. All means and standard deviations is smoothed with a 15 day running mean. As the data in the period after September 2004 was of a higher quality, the mean kinetic energy per unit mass was re-calculated after this time binned at $40m$ rather than $200m$.

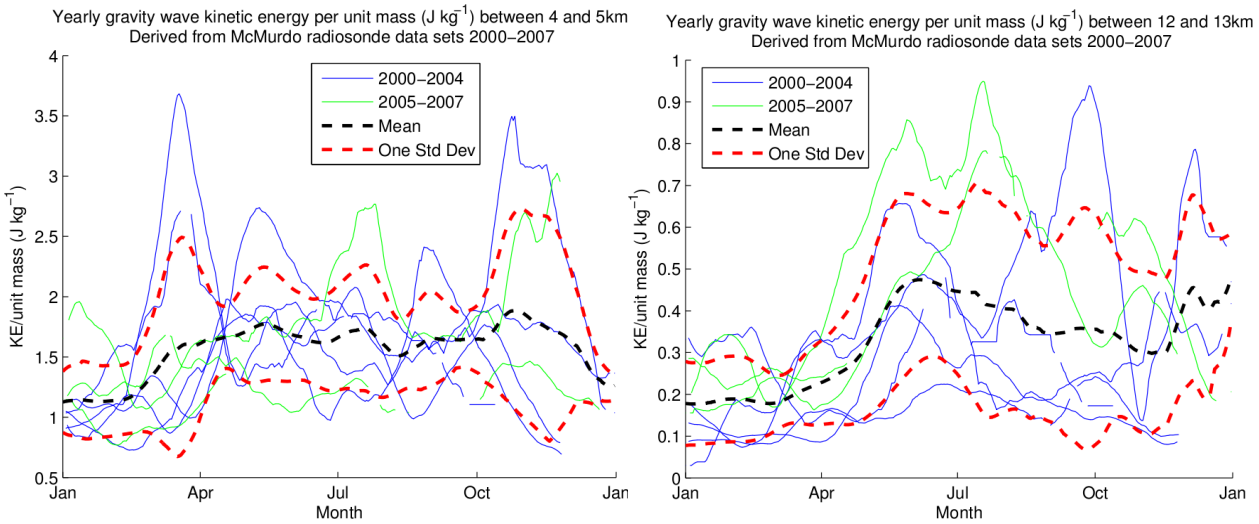

Figure 5.4: The mean gravity wave kinetic energy per unit mass in the troposphere in 2000-2007. In 2000-2004 the data quality was lower (detailed in Figure 5.1 and 5.2). The mean and standard deviation are smoothed with a 15 day running mean .

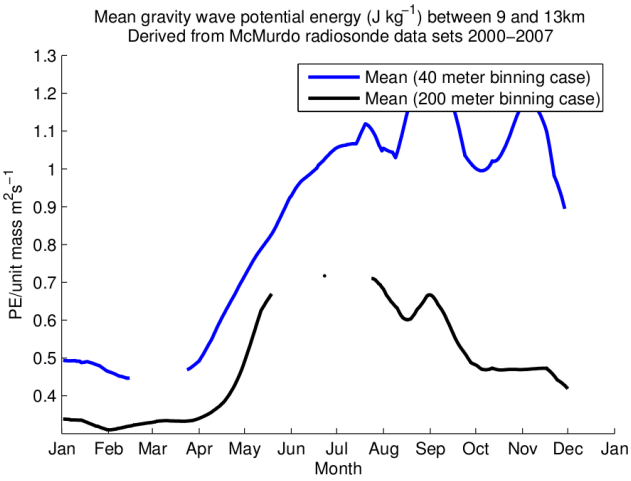

Figure 5.5: Potential energy associated with gravity waves between 9 and 13km. As the data in the period after September 2004 was of a higher quality, the mean kinetic energy per unit mass was re-calculated after this time binned at 40m rather than 200m.

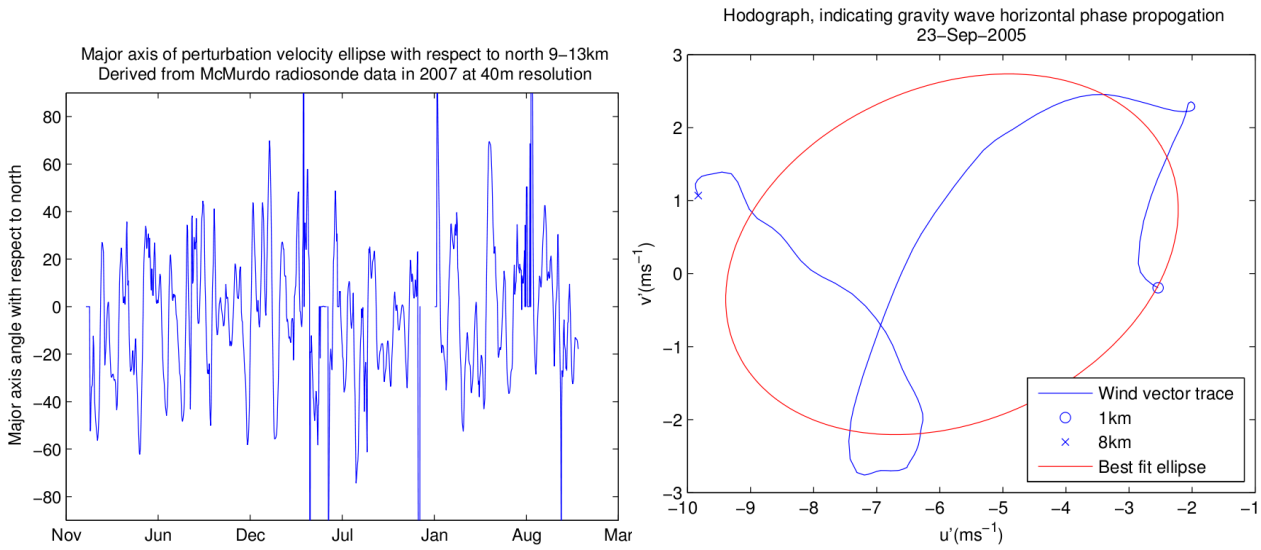

Figure 5.6: Mean gravity wave propagation direction between $1-8km$ and 2000-2007 with 15 day running mean. The graphic on the right is an example hodograph with a best fit ellipse. The linear fit approximates the major axis of the perturbation velocity ellipse. Note the the linear fit gives gravity wave propagation with 180°ambiguity.

of this wave is ENE or WSW due to the 180° phase ambiguity. Producing hodographs for each radiosonde launch and calculating the angle of the major axis of the best fit ellipse yields the diagram in left panel in Figure 5.6. This diagram shows that there is substantial variation in gravity waves propagation directions throughout the year. Therefore, when considering the gravity wave transfer function of the atmosphere in the following chapter, the possibility of gravity waves propagation in any direction should ideally be taken into account.

Note that the calculation of these hodograph ellipse major axis angles does not take into account radiosonde data sets where there is no clear gravity wave activity. These data sets manifest as hodographs with no discernible elliptical features. Hodographs of this nature may skew the propagation direction calculation. In future work, a quality control method should be used to ensure that the hodographs used have gravity wave features. This would potentially mean that the gravity wave propagation directions at the source would be reliable enough to include when considering the atmospheric transfer function. Hodographs also indicate whether a gravity wave is propagating up or down. The rotation in the hodograph of Figure 5.6 is anticlockwise; this indicates upward wave propagation in the southern hemisphere (*Vincent and Alexander*, 2000). In future work, information about gravity wave vertical propagation could also be used to only include radiosonde flight which include upward wave propagation in the gravity wave source function.

Comparing the effects of the atmospheric transfer function on these gravity wave climatologies with the high altitude MF-radar derived gravity wave climatology, the properties of the lower altitude gravity waves can be inferred.

Chapter 6

Model Derived Gravity Wave Filtering Scheme

As detailed in Section 3.3.1, a variety of conditions can prevent the vertical propagation of gravity waves. One of the more important of these mechanisms is critical level filtering. This occurs when a vertically propagating wave approaches a region where the background flow matches its intrinsic horizontal phase velocity. At this point, the wave will be absorbed into the background flow. It should be noted that under certain conditions gravity waves can penetrate critical levels (*Fritts*, 1978). In addition to directly penetrating the critical level, when size changes relatively rapidly due to tidal effects, the propagating gravity wave can have its phase velocity increased enough to pass by the blocking circle, effectively being "pushed" passed the critical level. For the purposes of this study, these two effects are considered to be small enough to not affect the overall picture of gravity wave filtering.

The primary velocity field data set used in this thesis to calculate gravity wave filtering was the Horizontal Wind Model 1993 FORTRAN (HWM 93) model described in *Hedin et al.* (1996). The HWM 93 is an empirical wind model based on a wide variety of data sets including rocket soundings, MF-radar winds, and meteor radar. This model was selected because it is easy to use and functions over a wide range of altitudes. In this case, it was used from 1-100km. The wave blocking calculated by this model was compared with data from the NCEP/NCAR reanalysis. The NCEP/NCAR data only goes as far as 30km, but the overlap with the HWM 93 model was sufficient to allow some comparison in filtering output.

The winds from the NCEP/NCAR and HWM 93 model were initially taken as daily averages. However, this can hide the strong wind variations which can occur at some altitudes due to waves such as the diurnal and semi-diurnal waves. This can result in waves appearing to be blocked when in fact they can by pass though at certain times in the day (*Zhong et al.*, 1996). As such, it was decided to use a time resolution of 15 min from the HWM 93 model, despite the significantly higher computational expense.

Critical level filtering was examined using the concept of a blocking circle (*Taylor et al.*, 1993). From Chapter 3, the blocking circle is given by

$$\Omega = \omega \left(1 - \frac{U \cos\phi + V \sin\phi}{\nu_x} \right) \tag{6.1}$$

where Ω is the Doppler-shifted velocity of the gravity wave in question. U and V are the zonal and meridional wind components respectively, and ϕ indicates the horizontal direction of wave propagation and ν_x its phase speed. Based on background flow given by U and V, the gravity wave with properties ω , ϕ and ν_x will be considered blocked if Ω is less than zero (*Taylor et al.*, 1993). Graphically, this results in a circle of radius $\sqrt{U^2 + V^2}$ centred on the Cartesian coordinates (U, V) shown in Figure 6.1. If a gravity wave's horizontal propagation direction and phase speed are within this circle, it will be unable to propagate any further vertically. Thus, these circles identify portions of the parameter space through which waves cannot propagate to higher altitudes.

All the data sets which were analysed to determine critical levels were divided into vertical height bins. Each day of data was successively examined for filtering. Blocking was determined by "looking down" from a certain height bin to those below it and creating a composite blocking circle based on all the blocking circles below (and including) the altitude bin in question (see Figure 6.2). The degree of wave blocking is obviously dependent on the maximum phase speed specified. This defined a circle with a radius of the maximum phase speed (the thick black outer circle in Figures 6.1, 6.2 and 6.3). The area of this circle removed by the composite blocking circles determines the percentage of waves blocked.

Often, composite blocking circles will have simple geometries. This is due to the wind field slowly increasing or decreasing with altitude and the generally weak meridional component of the wind (particularly in the Antarctic). However, in regions where tidal and gravity wave amplitudes are large, they can cause the blocking circles to rotate around the origin as altitude increases. This can lead to relatively complicated composite circles; even the three altitude bin composite blocking circle displayed in Figures 6.2 and 6.3 would be somewhat challenging to evaluate in a computationally efficient manner. Therefore, a Monte Carlo integration method was chosen to determine the degree of blocking due to critical levels.

6.1 Monte Carlo integration of composite blocking circles

The Monte Carlo method of integration is based on random numbers. In a simple two dimensional Cartesian case, random points are spread over an area of interest and each random point is checked in order to determine if it is under the function being integrated (see Figure 6.4). The fraction of random points falling under the function of interest is related to the integral. *Press* (1986) gives the equation for Monte Carlo integration as

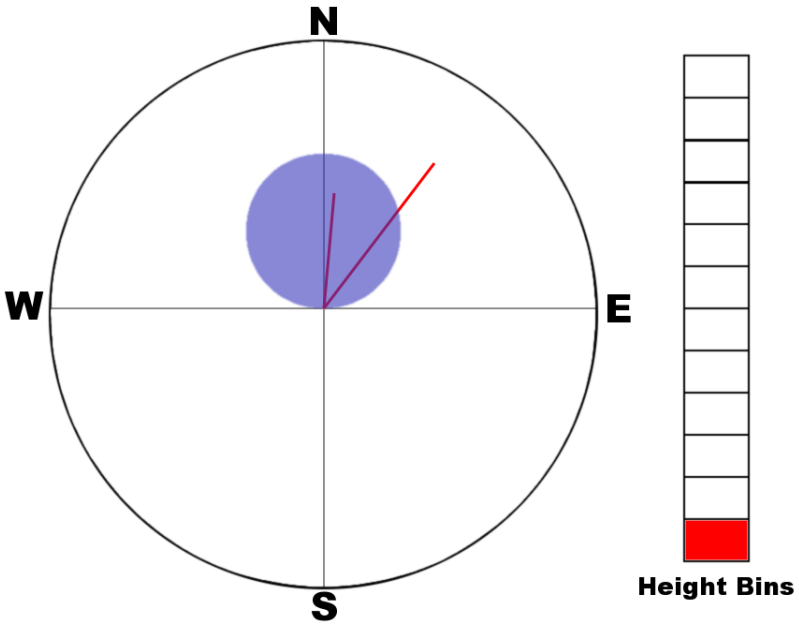

Figure 6.1: Fictional blocking circle in the lowest height bin due to a meridional wind blowing directly toward the north (northward) with no zonal component. The blue circle represents the range of phase speeds and wave directions that will be unable to pass through this altitude. The red lines represent gravity waves with certain phase speeds and horizontal directions. The wave inside the blocking circle will be unable to propagate higher while the other wave has a sufficient phase speed to pass through the potential critical level.

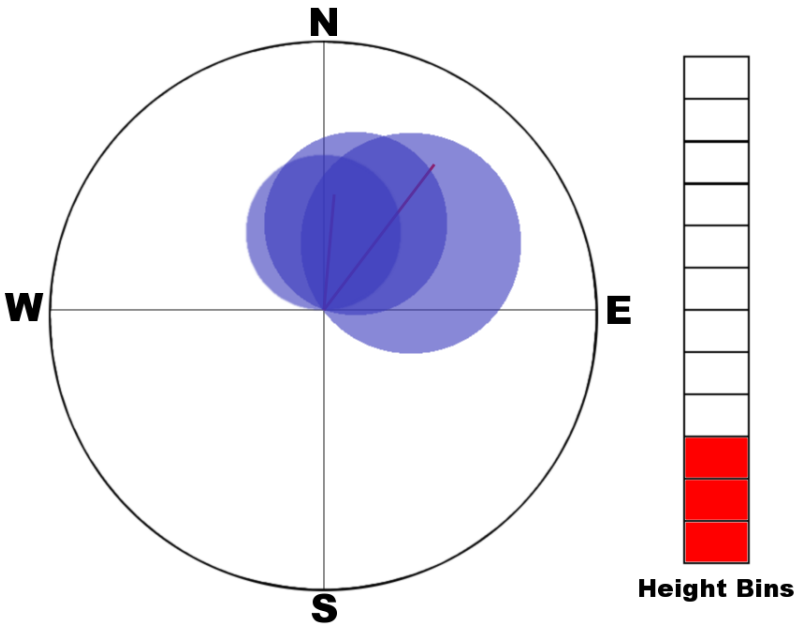

Figure 6.2: Composite blocking circles "looking down" from the third height bin on a certain day or time period. As successively higher altitudes are examined the meridional wind component grow weaker while a eastward wind strengthens. This can be seen by the coordinates of the successive blocking circles (U, V) It can be seen that the gravity wave which was able to pass through the first and second bins reaches a critical level by the third bin and is stopped.

$$\int f dA \approx A\langle f\rangle \pm \sqrt{\frac{\langle f^2\rangle - \langle f\rangle^2}{N}} \tag{6.2}$$

where $\langle f\rangle \equiv \frac{1}{N}\sum_{i=1}^{N} f(x_i)$ and $\langle f^2\rangle \equiv \sum_{i=1}^{N} \frac{1}{N} f^2(x_i)$

f is the function being integrated, N is the total number of random numbers generated, and A is the area under consideration – in our case, the circular area defined by the maximum phase velocity being considered. This can be seen in Figure 6.4 as the area comprised of the blue dots. x_i is each random point. The plus and minus term in equation 6.2 is an estimate of one standard deviation for the integral.

Equation 6.2 can be modified to conform to the specific case of gravity wave filtering. As the fraction of the wave being blocked is what is of interest, the term V can be dropped, giving the fraction of points inside the integral.

$$\int f dA \approx \frac{1}{N}\sum_{i=1}^{N} f(x_i) \tag{6.3}$$

Equation 6.3 can be applied to determine the fraction of waves blocked by composite blocking circles. In this case, area A will be a circle determined by a chosen maximum phase speed and random numbers will be generated in polar coordinates (v_x, ϕ), and tested against equation 6.1. Note that particular care has to be taken in the generation of a uniform distribution of random points in polar coordinates. Simply generating a random radius and angle will result in the random points clustering predominantly around the origin. In this study, random polar points were first generated in a Cartesian space; if they fell inside the circle defined by the maximum phase being tested they were then transformed into polar coordinates. This ensured a uniform random distribution for the Monte Carlo integration.

The number of random points used in the Monte Carlo points would clearly have an impact of the quality of the calculated wave blocking, with more points producing a better result. However, the number of random points generated had a large impact on the computational requirements of the calculation. To determine the number of points giving a balance between calculation time and computational quality, a series of runs using different numbers of random points were compared to a run using ten million points. The ten million point run was taken to represent the true result. Several runs using this many points all gave very similar results. A run with a large number of points was used instead of an analytical solution to allow testing of various days and height bins more easily.

The results of the tests against ten million points is shown in Figure 6.5. Repeated tests at different points, different altitude bins and different maximum phase speeds all gave similar results. From this, it was determined that ten thousand points would give results to within one standard deviation of 1% from the ten million point case, and two standard deviations from the 2% difference.

To determine the degree to which the composite blocking circles prevented upward wave propagation, it was necessary to choose a maximum wave phase speed to consider. Diagram-

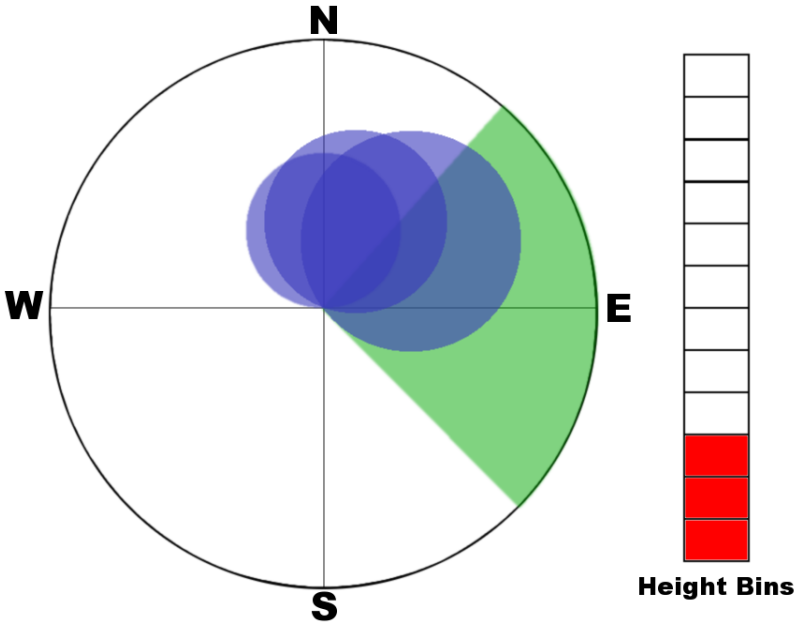

Figure 6.3: By restricting the Monte Carlo random numbers to the eastward quadrant, the blocking of waves propagating in the eastward direction could be studied. By repeating this for the remaining cardinal directions and a range of maximum phase velocities it is possible to identify a relatively comprehensive overview of wave blocking.

matically, this gives the maximum area which the blocking circles can cover. If 100% of this area were covered by blocking circles, no waves with a phase speed equal to or less than the chosen maximum phase speed could propagate past this level. A variety of phase speeds were used to help determine what proportion of waves of different phase speeds might be affecting the gravity wave climatology observed by the MF-radar. For instance, if a maximum phase speed of $5ms^{-1}$ was considered and it explained the observed wave field, then it would be reasonable to assume that large phase speed waves were rare. The relative contribution of waves for different ranges of phase speeds should provide valuable information about the sources of the gravity waves.

A particularly powerful feature of using the Monte Carlo method is that it makes it easy to test for blocking in certain directions by only picking random points in a sector. This can be seen in Figure 6.3; the green sector shows the area the random points are being restricted to. In this example, the blocking of waves which only propagate in the eastward direction were considered. Studying all four cardinal directions at a range of maximum phase velocities allows a comprehensive overview of wave blocking during the year. Averaging a range of years together allows a blocking climatology to be developed for a range of different maximum phase speeds and propagation directions.

Initially, it was planned to generate a new set of random points at each level. This would have had the advantage of allowing the blocking at each specific height bin to be examined individually. Using this information, it would have been possible to gain an understanding of strong blocking layers overlying lower levels of blocking. If, as assumed, gravity waves were only propagating from the lower troposphere directly below the blocking level, this would not provide more insight into gravity wave blocking. However, if gravity waves were either horizontally infiltrating the observed region above the lower level filtering or being

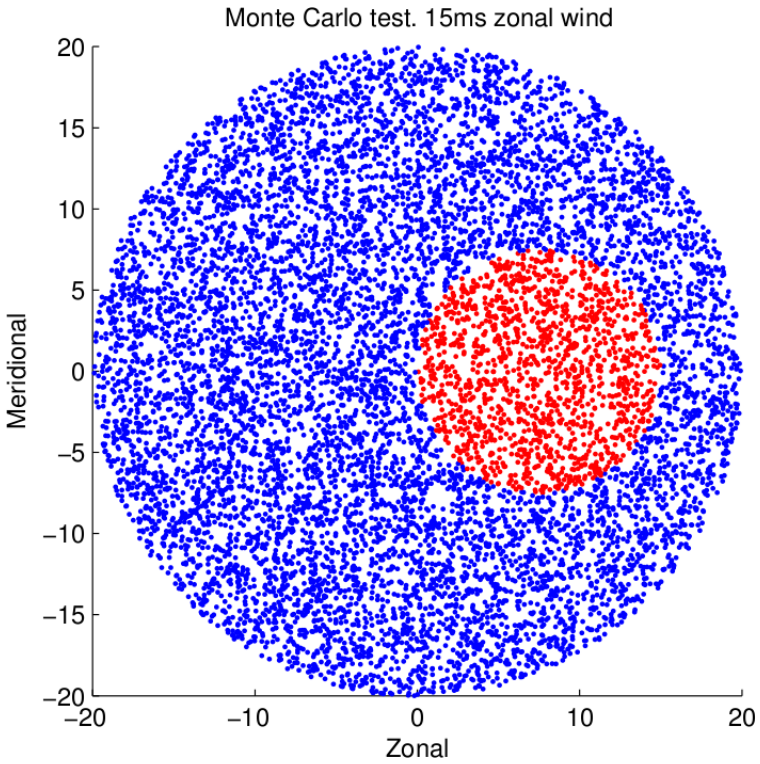

Figure 6.4: A test of the Monte Carlo method using equation 6.3 and a background wind of $15ms^{-1}$ toward the east (the right hand side of the diagram). The points are random phase speeds with a maximum phase velocity of $\pm 20ms^{-1}$ and a random propagation direction. The red points are considered blocked by equation 6.3. The fraction of waves blocked in this example is 0.14 or 14%

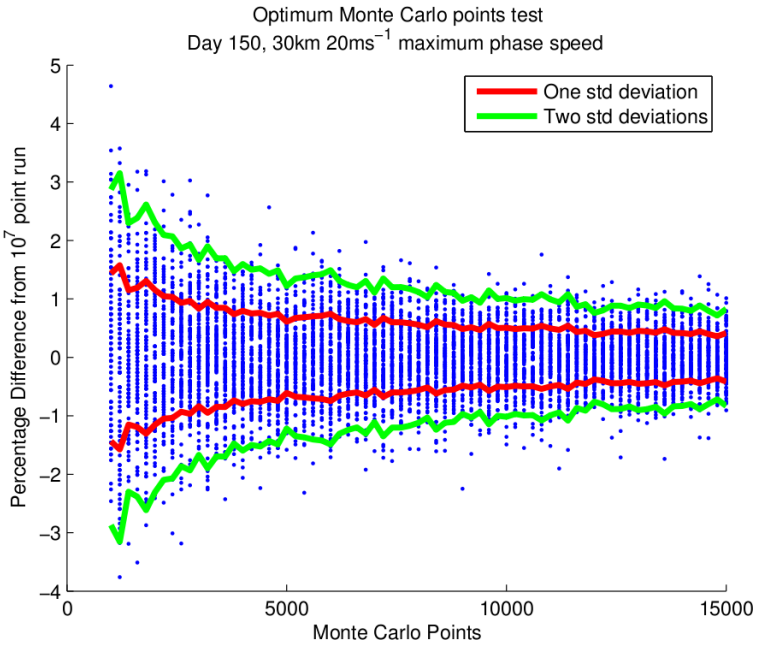

Figure 6.5: Testing for the optimum number of points for the Monte Carlo wave blocking calculation. The blue points represents how close each run was to an ideal case. The ideal case was taken to be the result of a ten million point run. Each run used a different number of randomly generated points, repeated 100 times to obtain a meaningful spread of points. The red line and green line show one and two standard deviations in difference respectively.

generated at altitude, this additional information about overlying gravity filtering could be useful. Unfortunately, this proved to be very computationally expensive. We therefore generated one set of random points for the lowest bin and removed the points representing wave phase speeds and directions blocked from the random point set. This set of random points was then moved up each altitude bin and the remaining points tested for blocking. The rational for this was, assuming all the gravity waves propagated from the lower troposphere, waves blocked at lower levels would remain blocked at higher ones. This modification of the use of random points greatly sped up computation, enabling the examination of a variety of phase speeds and wave blocking directions.

6.1.1 Radar winds/HWM 93 hybrid filtering scheme

In an attempt to improve the resolution of the atmospheric transfer function, the transfer function calculated using the HWM 93 model was modified with a calculation of gravity wave blocking using wins from the Scott Base MF-radar. The blocking due to radar winds was calculated from $70km$ assuming the blocking below this level was the same as that calculated using the HWM 93 model

In order to correctly deal with the blocking fractions, the radar data was modified using the model blocking at the radar's lowest altitude bin, in this case $70km$. To do this, the model blocking at $70km$ was transformed into the fraction of waves passed. Multiplying this by the radar blocking gave additional waves blocked at a particular height bin. Adding this fraction to the model blocking at $70km$ yielded a hybrid blocking fraction

$$H_B \quad = \quad M_{70} + R_B \left(1 - M_{70}\right)$$

where H_B is the hybrid blocking fraction, R_B is the radar winds derived blocking fraction and M_{70} is the HWM 93 model derived blocking fraction at $70km$.

6.2 Mountain wave specific filtering

The blocking circle described above can be modified to determine wave blocking acting specifically on mountains waves. This is an important step as there is good reason to believe that much of the gravity wave activity in the Scott Base region will be due to topographically generated mountain waves (see Chapter 3 and *Baumgaertner and McDonald*, 2007).

Topographically generated gravity waves (or mountain waves) ideally have a phase speed of zero. Setting the maximum phase speed to zero in the standard blocking circle method will clearly not work[1]. Therefore, this method needs to be modified to determine the degree of filtering associated with waves of zero phase speed efficiently.

In this case rotation of the background wind field is clearly important. Background winds will block any small phase velocity waves 90° to either side of its vector. As such, wind rotations of 180° between any two given heights block all zero phase velocity waves

[1]Note: It would be possible to use an arbitrarily small phase velocity, however this would be computationally inefficient

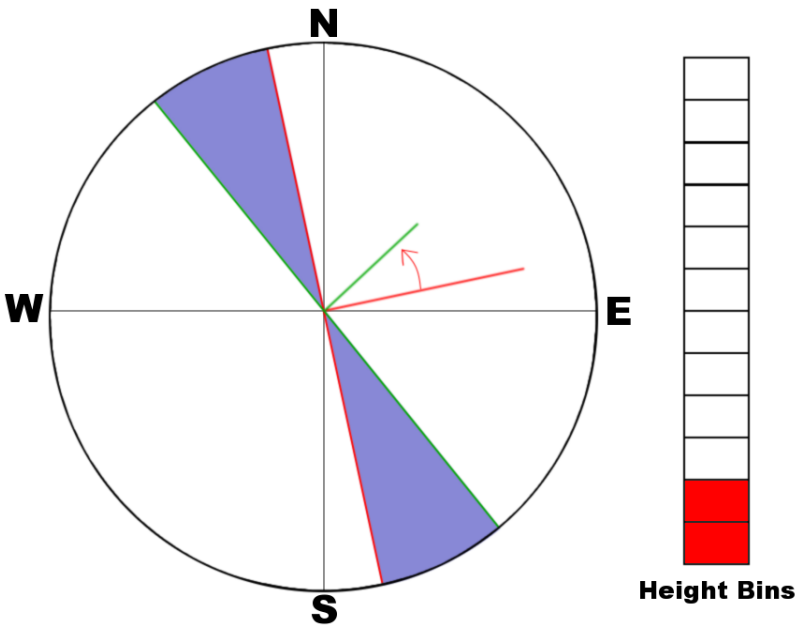

Figure 6.6: The blocking of small phase velocity waves as the wind vector rotates between two height bins. The red line indicates the wind vector in the first altitude bin while the green indicates the wind vector in the second bin. The shaded area indicates the degree to which low phase velocity waves are blocked.

(*Whiteway and Duck*, 1996). Rotations less than 180° will block corresponding less waves. This principle is illustrated in Figures 6.6 and 6.7.

6.3 Results

An examination of the wave filtering via the HWM 93 model is shown in Figures 6.8 - 6.10. The most prominent feature in all the diagrams is a general increase in wave blocking with altitude. This would be expected, since waves blocked at low altitudes remain blocked at higher altitudes. This, combined with variations in wind speed and direction with altitude, would lead to increased blocking with altitude.

Secondly, the low phase speed waves are blocked far more than higher phase speed waves. The blocking of low speed waves occurs over a larger period of the year, and the blocking is more pronounced with height. A particularly clear example of this is the filtering of eastward propagating waves between 0 and $5ms^{-1}$ displayed in Figure 6.8. In this case, eastward propagating waves are almost completely prevented from vertically propagating, whereas in the case of phase speeds up to $20ms^{-1}$ the eastward waves can strongly propagate up to $100km$ during the summer months. This result is expected, since low speed waves are more likely to be inside a blocking circle at a particular altitude.

Another notable feature of the HWM 93 wave blocking diagrams was the strong seasonal patterns. There was a strong difference between the low maximum phase speed case (Figure 6.8) and the higher maximum phase speed cases (Figures 6.9 - 6.10). Looking firstly at the higher phase speed cases, the strongest overall blocking occurred during the winter months, with the $20ms^{-1}$ case showing stronger blocking than the $40ms^{-1}$ case. Around the March

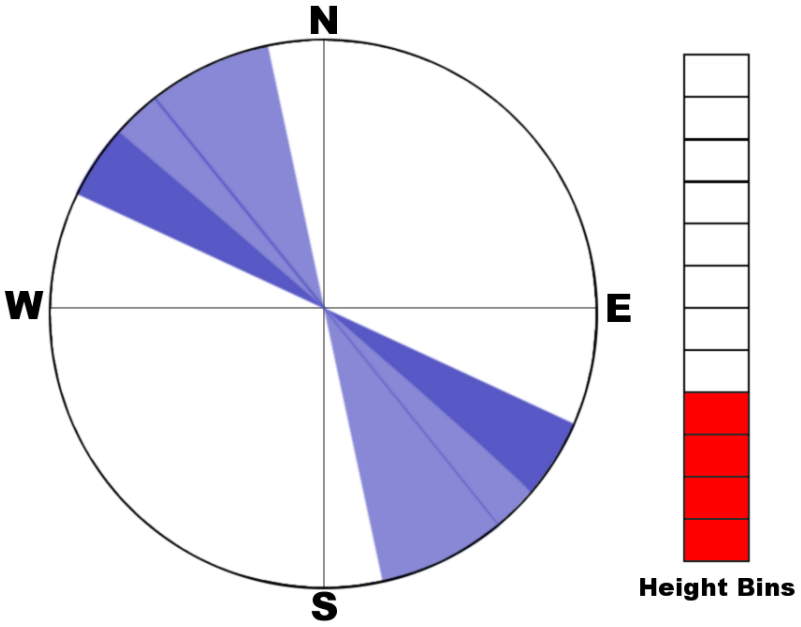

Figure 6.7: Blocking of small phase velocity gravity waves between 4 altitude bins. Note that between the 3^{rd} and 4^{th} height bin the wind vector starts to move back toward the direction of wind in the second height bin. These reversals need to be taken into account .

and September equinoxes there was significantly more wave penetration than during the rest of the year.

Dowdy et al. (2007) used exclusion circles to identify the effect of gravity wave filtering on observations from Davis ($69°S, 78°E$) and Syowa ($69°, 40°E$) stations. Their results are shown in Figure 6.11. While Davis and Syowa are further from the pole than Scott Base, the gravity wave filtering should be broadly similar. *Dowdy et al.* (2007) shows particularly strong blocking of eastward waves during winter and particularly weak blocking of westward waves during summer at both locations. All results are consistent with the results obtained for Scott Base.

The reason all three bases show similar gravity wave blocking is the change in direction of the Antarctic stratospheric jet. During the winter months, eastward propagating waves are very strongly filtered by the eastward polar night jet, with higher phase speed waves having better penetration. During the summer months, the weaker westward stratospheric jet filters westward propagating waves, albeit to a lesser extent both in time and altitude than the winter jet. During the equinoxes the stratospheric jet is changing direction. This implies a weakening as well as a degree of variability in the wind field. This weaker zonal wind field produces small blocking circles, allowing waves with faster phase speeds relatively unimpeded access to the upper atmosphere.

The main wind feature in the polar atmosphere is the zonal jets; the meridional wind field is much weaker and less variable. For this reason, the blocking of northward and southward waves in the $0 - 20ms^{-1}$ and $40ms^{-1}$ maximum phase speed cases was primarily due to "ghosting" of the eastward and westward filtering. This occurred as a result of the blocking circles associated with strong eastward and westward winds extending into the sector defined as northward or southward blocking. This is not to say that there was no

blocking of northward and southward propagating waves, only that at higher phase speeds this blocking was dominated by eastward and westward winds.

The lower maximum phase speed blocking diagrams, $0-1ms^{-1}$ and $0-5ms^{-1}$ (Figures 6.8 and 6.12) display quite a different seasonal pattern. The equinox gaps in the blocking field associated with higher speed waves are replaced by regions of stronger blocking. While the winds during the equinox are not particularly strong, they are highly variable in both direction and speed. This variability makes it far more likely for the phase speed and direction of a propagating gravity wave to be matched, hence filtering the wave out. These low maximum phase speed cases are very similar to the wave blocking as calculated by rotation alone (Figure 6.13).

The wave blocking determined using wind rotations as well as the low phase speed cases mentioned above indicate that mountain waves, which have phase speeds close to or equal to zero, would not be able to propagate vertically very well during the summer months between the equinoxes.

In order to determine how well the gravity wave filtering scheme based on the HWM 93 model matched real world data, it was compared to a gravity wave filtering scheme based on the NCEP/NCAR reanalysis data, using the same techniques. The NCEP/NCAR data is a combination of observations and short term weather forecasts (*Kalnay et al.*, 1996). As such, this data is likely to be a closer representation of reality than the HWM 93 model in its height range. Unfortunately, this data only extends to $30km$ and hence cannot be used to generate the full gravity wave filtering scheme. The features of the model gravity wave filtering were broadly similar to the NCEP/NCAR gravity wave filtering. However, Figure 6.14 clearly shows that while the overall magnitude of filtering was similar, the NCEP/NCAR gravity wave filtering field had more high frequency detail, particularly in midwinter.

Lastly, the HWM 93 gravity wave filtering field was used with radar derived gravity wave filtering fields to create hybrid filtering fields. This has the advantage of producing a wave blocking field with far more features than the pure HWM 93 blocking. An immediately obvious problem with this method is saturation (Figures 6.15 and 6.16); the strong bands of filtering in the eastward and westward filtering fields is an artifact caused by strong filtering calculated using the HWM 93 model. However, away from the saturation band, the hybrid filtering shows far more features than blocking derived using only the HWM 93 model.

Apart from the saturation bands, the other particularly interesting difference between the hybrid blocking and the pure HWM 93 blocking is the relatively strong blocking of north and south propagating waves in the lower phase speed cases. Some of this will be due to the ghosting effect described previously, however its general features suggest that this is not the only effect. Figure 2.5 shows that in the region of 70-100km the meridional winds can be much closer to the zonal wind speeds than at lower altitudes, particularly in winter, which could well be the cause of much of the north/south blocking at low phase velocities.

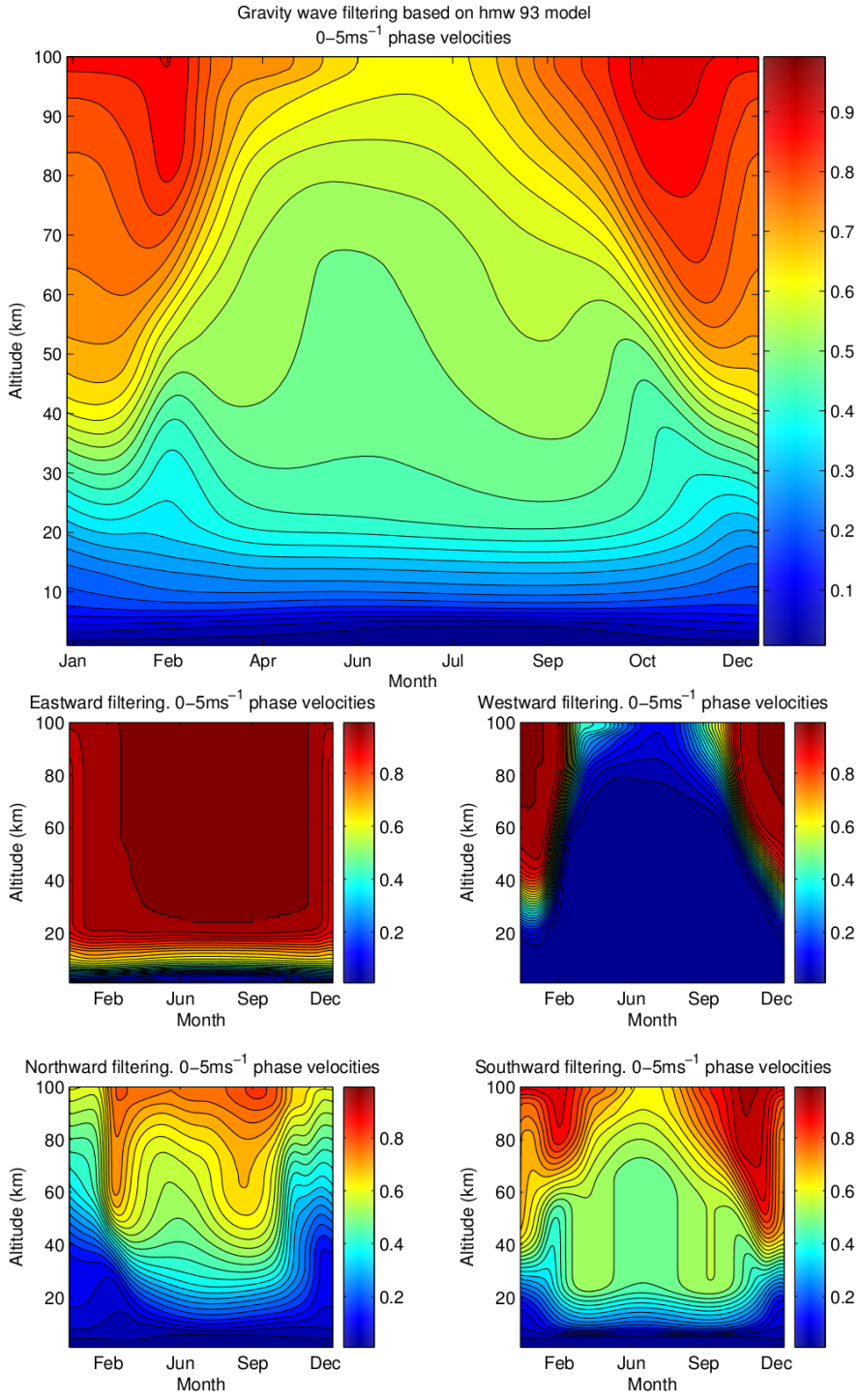

Figure 6.8: Filtering scheme for gravity waves with a phase speed between 0 and $5ms^{-1}$. The lower panels show the blocking field separated into NSEW filtering components.

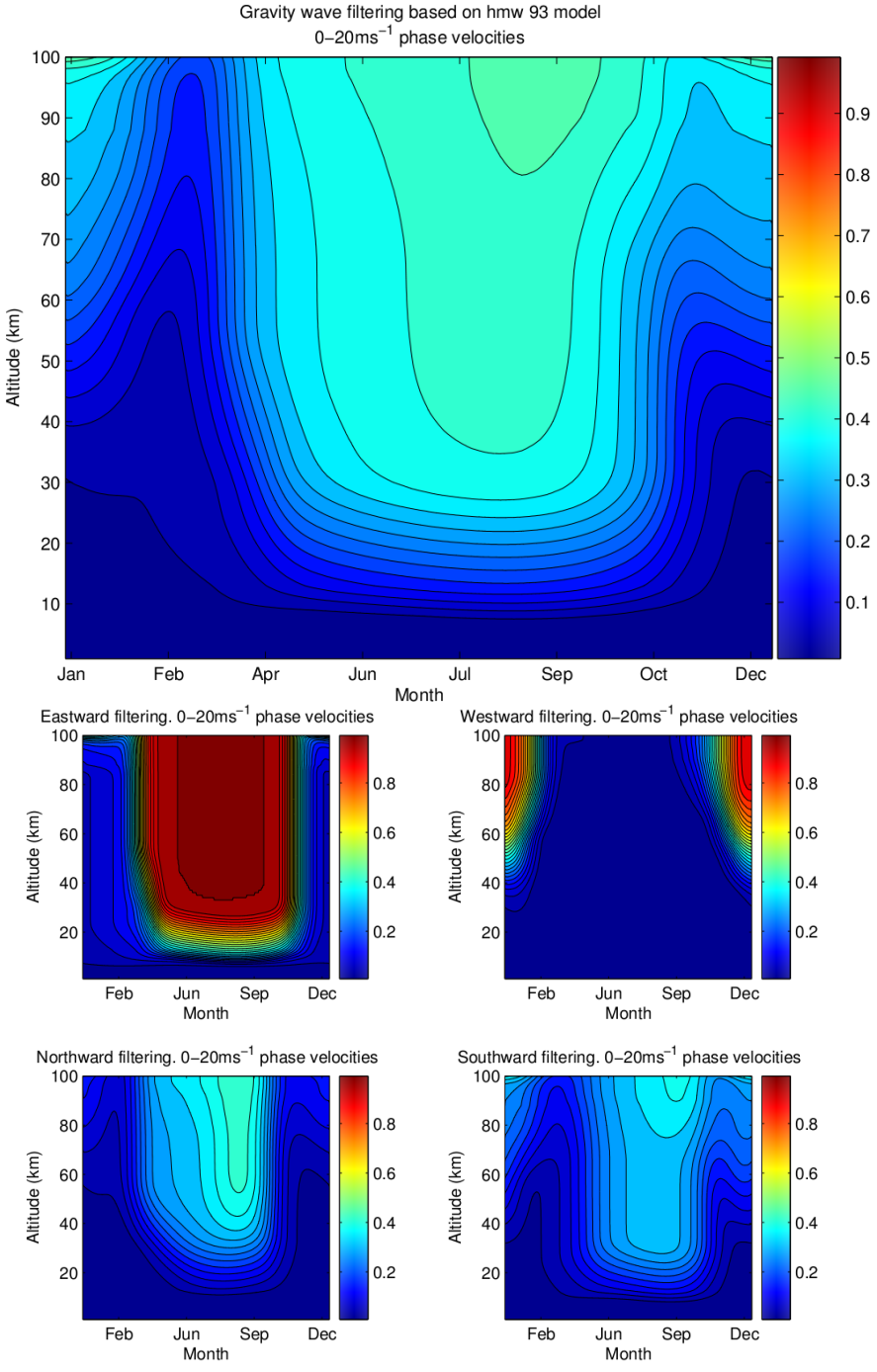

Figure 6.9: Filtering scheme for gravity waves with a phase speed between 0 and $20ms^{-1}$. The lower panels show the blocking field separated into NSEW filtering components.

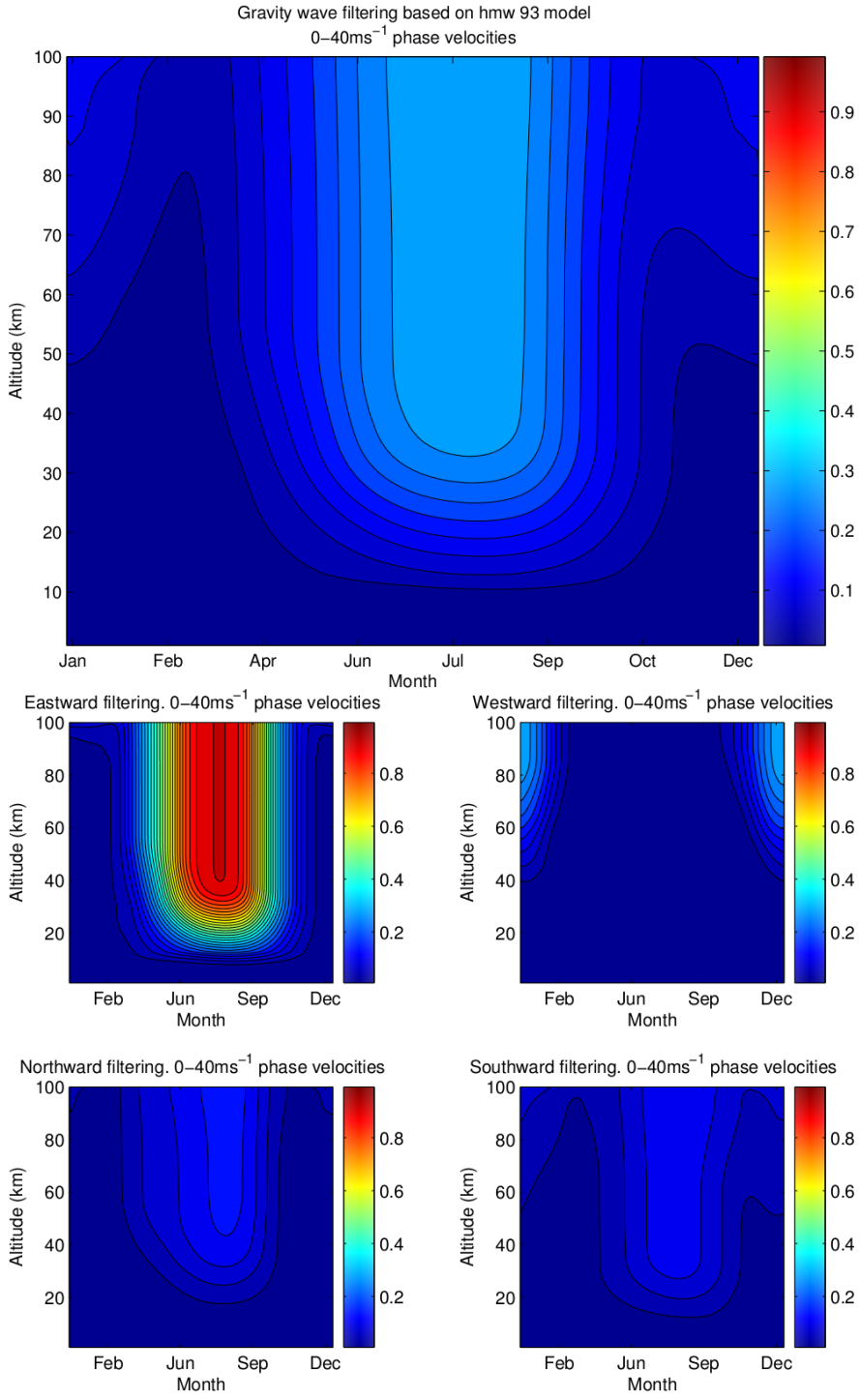

Figure 6.10: Filtering scheme for gravity waves with a phase speed between 0 and $40ms^{-1}$.The lower panels show the blocking field separated into NSEW filtering components.

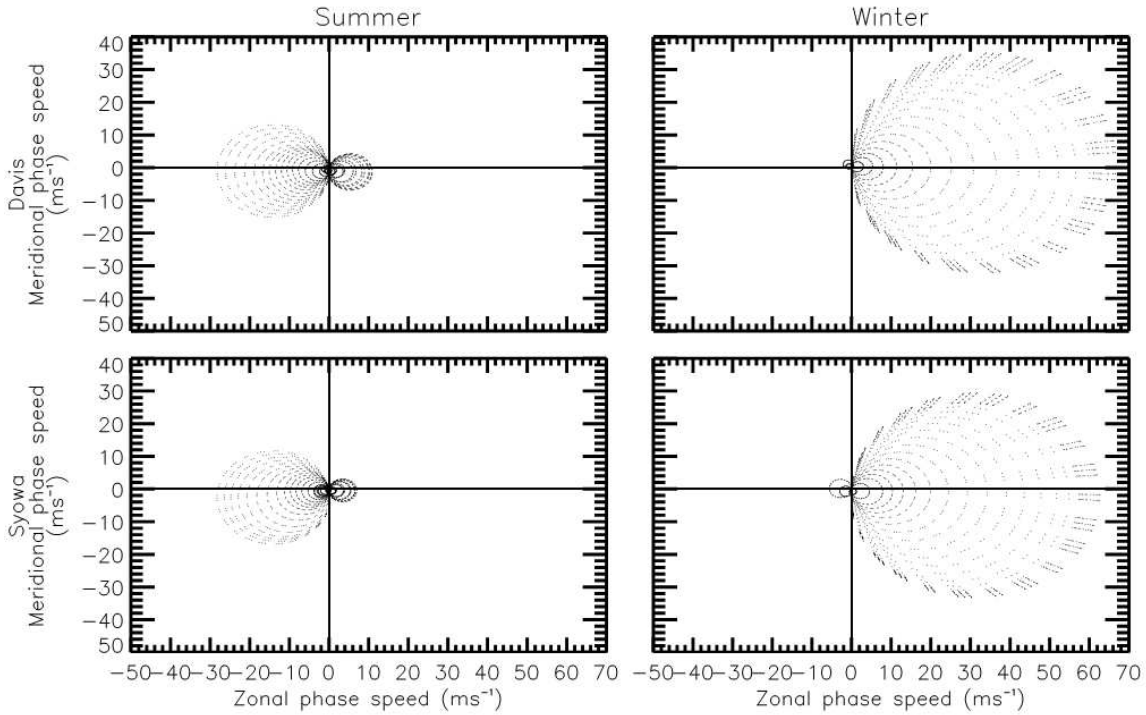

Figure 6.11: Summer and winter gravity wave blocking circles at Davis ($69°S, 78°E$) and Syowa ($69°, 40°E$) stations. Calculated from the ground up to approximately $56km$. From *Dowdy et al.* 2007 (Modified to show Antarctic locations only)

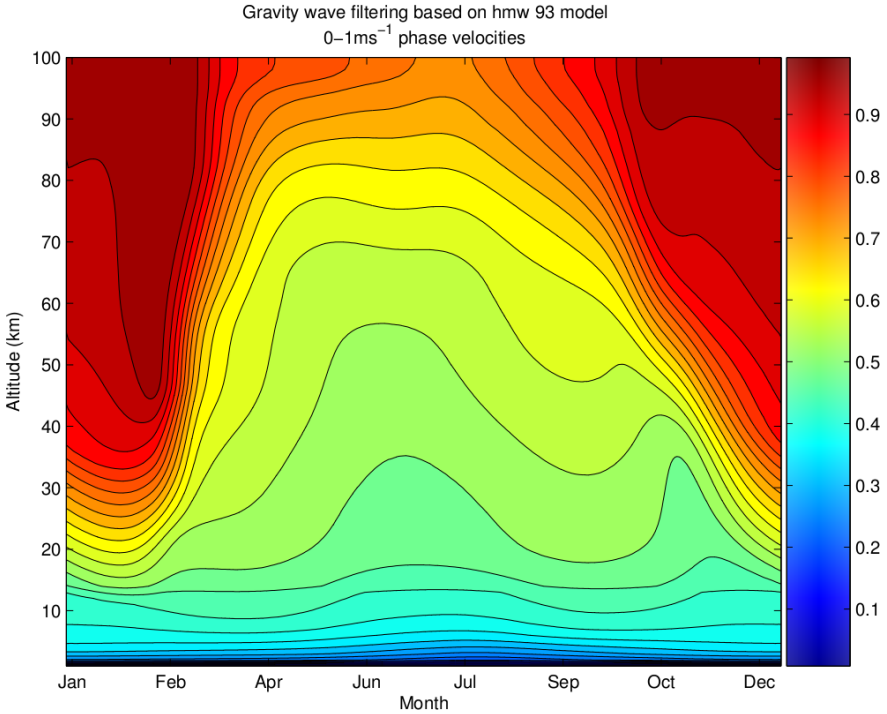

Figure 6.12: Filtering scheme for phase speeds between 0-1ms^{-1}. This should be representative of mountain wave filtering.

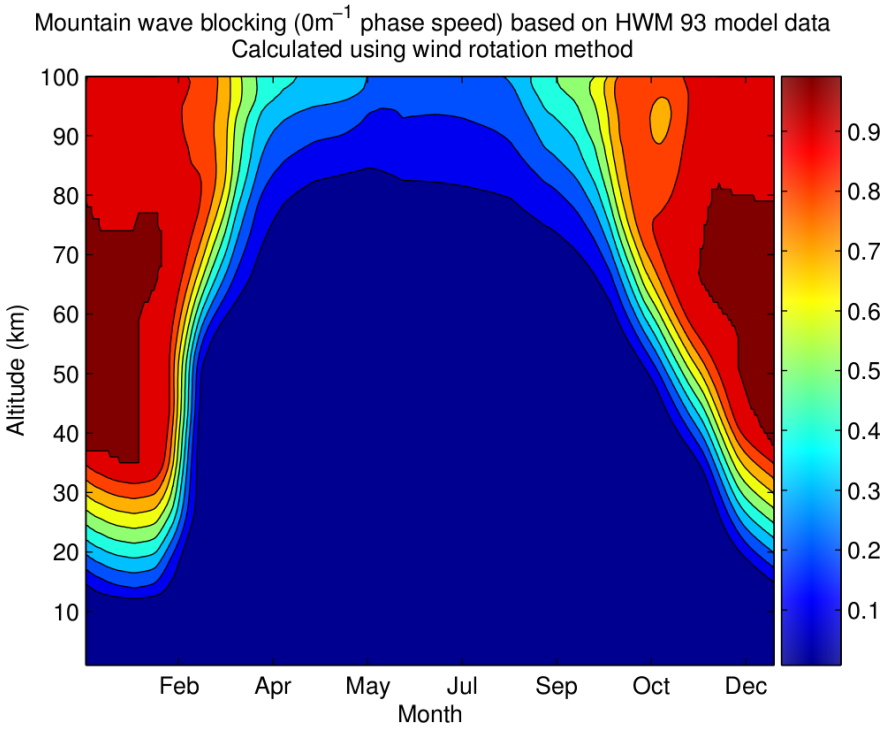

Figure 6.13: Filtering scheme based on wind rotations. The wind field is checked for rotations of more than 180 degrees from the ground up. Where this has occurred mountain waves are considered completely blocked. Lesser degrees of rotation are shown as a fraction of 180 degrees rotation.

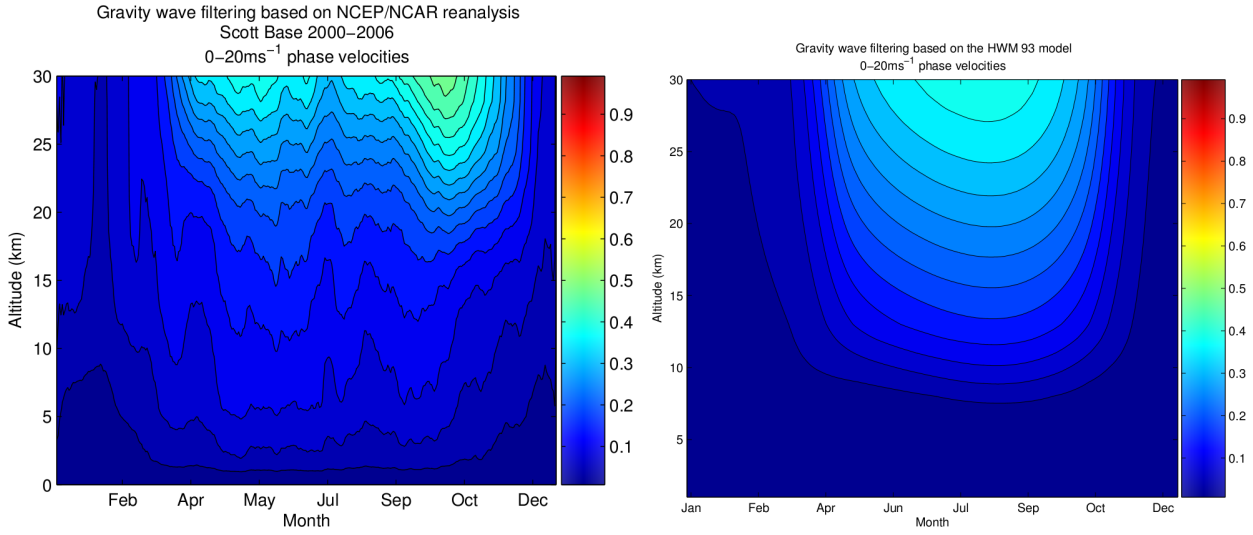

Figure 6.14: NCEP/NCAR reanalysis based gravity wave blocking between 0 and 20 ms^{-1}

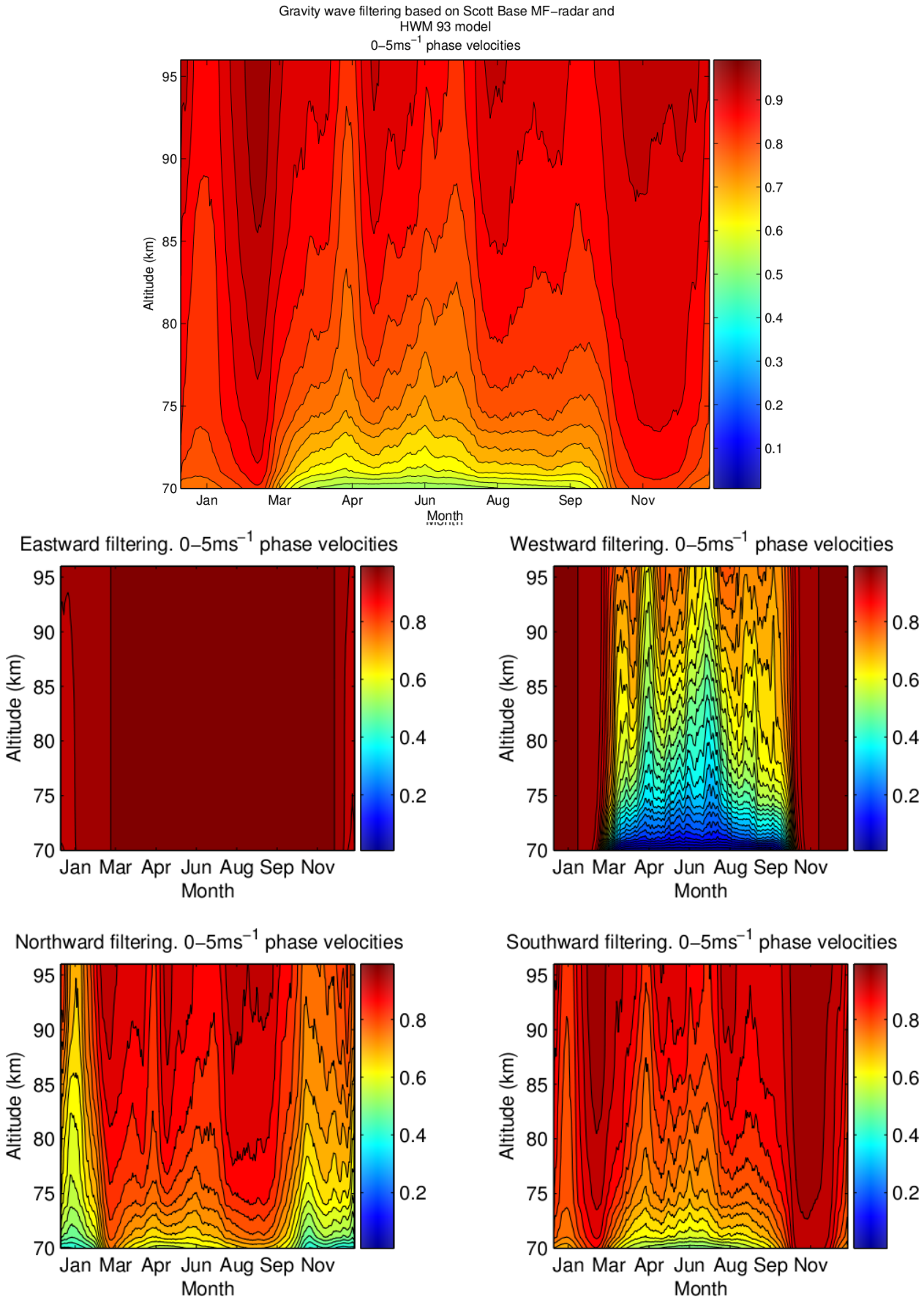

Figure 6.15: Hybrid filtering scheme for phase speeds between 0-5ms^{-1}

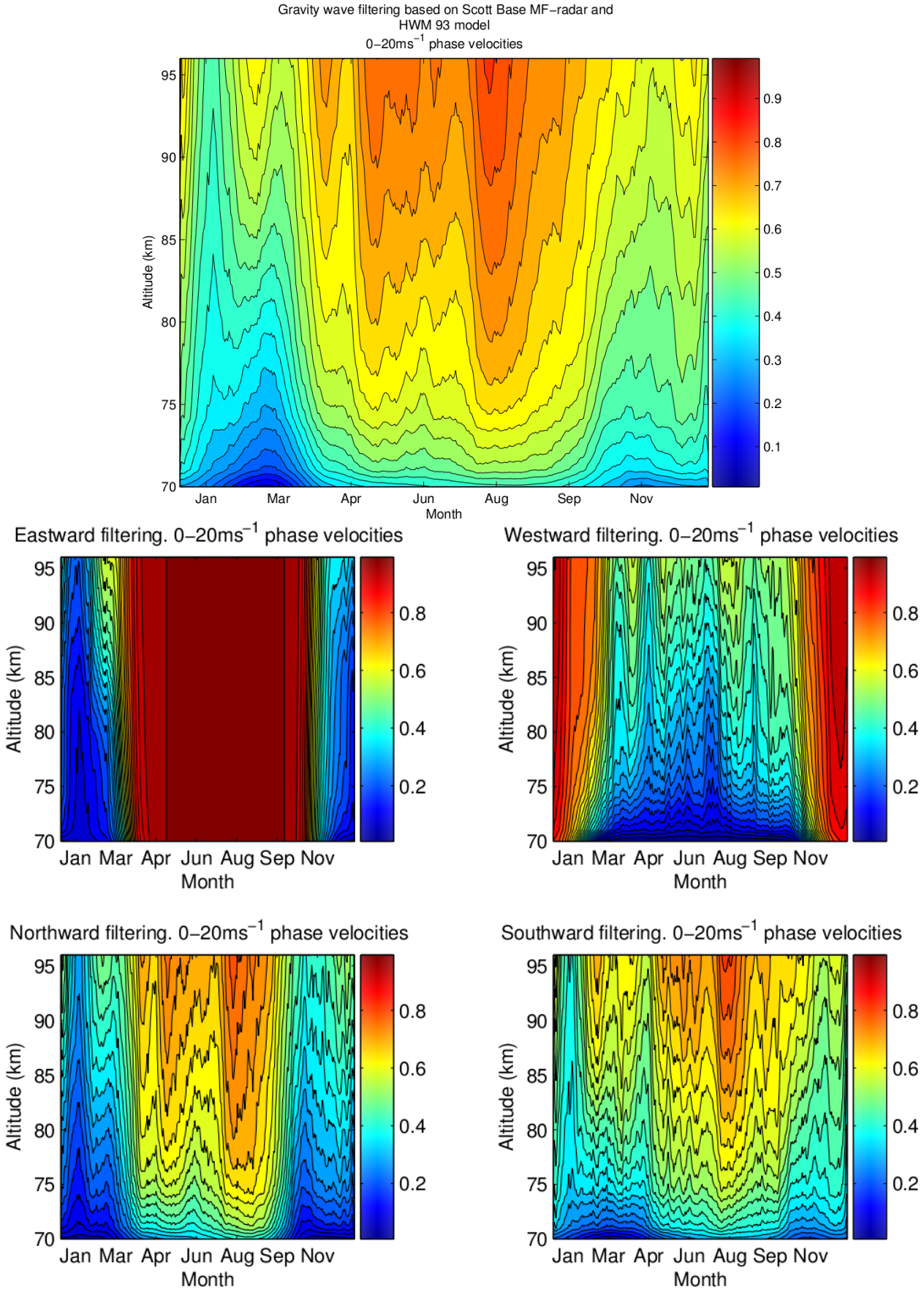

Figure 6.16: Hybrid filtering scheme for phase speeds between 0-20ms^{-1}

Chapter 7

Least Squares Fitting the Transfer Function

7.1 Introduction

In this chapter, the gravity wave source function (Chapter 5) and the gravity wave filtering scheme (atmospheric transfer function, Chapter 6) are fitted to the observed MLT gravity wave climatology (Chapter 4). The quality of the fits, determined by the norm of the residual, can be used to infer some basic properties of the observed MLT gravity wave field and the atmospheric transfer function above Scott Base.

7.2 Methodology

The atmospheric transfer function was designed to filter waves propagating in the four cardinal directions, as well as in more general cases when propagation direction was ignored. By examining the filtering of waves propagating in different directions, it will be possible to obtain some information about the likely composition of the observed MLT gravity wave field. For instance, if it is observed that waves propagating in all directions except eastward are blocked at a particular time of year, and gravity wave activity is still strong, then it can be surmised that the gravity wave source contains a large proportion of eastward propagating waves.

A similar argument can be made for phase velocities; if only high phase speed waves can pass into the mesosphere, and strong gravity wave activity is also observed, then it is reasonable to assume that topographic gravity waves do not contribute strongly to the wave field, as these would have a phase speed close to zero. However, it could be possible to observe strong activity when all reasonable phase speeds and directions are blocked. This could indicate that gravity waves are being generated above critical levels (e.g., from jet sources), or perhaps waves are infiltrating the observed region horizontally.

The gravity wave field observed in the mesosphere is assumed to be caused entirely by the low altitude gravity waves (represented by the gravity wave source function), the action of

critical level filtering, and an assumed exponential growth in wave amplitude with altitude. The exponential wave growth results in kinetic energy at a certain altitude being related to the kinetic energy at higher altitudes, according to equation 7.1 (adapted from (*Dowdy et al.*, 2007))

$$E_{k_H} = E_{k_L} e^{z/H_\rho} \tag{7.1}$$

where E_{k_H} is kinetic energy at a greater altitude (in this case the MLT gravity wave climatology); E_{k_L} is the kinetic energy at the source (the radiosonde derived gravity wave source function); z is altitude in km, and H_ρ is the density scale height.

To account for the atmospheric transfer function, Equation 7.1 is modified to

$$E_{k_H} = A S_F W_P e^{z/H_\rho} \tag{7.2}$$

where S_F is the source function kinetic energy; W_P is a wave passing function (one minus the atmospheric transfer function blocking), and A is a fitting parameter. The least squares fitting is done for each day of data, fitting equation 7.2 to the gravity wave kinetic energy height profile. In addition, the atmospheric transfer function is calculated for a series of different phase speed ranges, each of which is independently used in each daily fit. The fits also use source functions at two different altitudes; an average source function from 1 - $8km$ encompassing the troposphere, and 9 - $13km$ corresponding to the Antarctic tropopause in summer. Initially, it was intended to fit for atmospheric transfer functions in the four cardinal directions, but unfortunately the north and south transfer functions are far from independent of the east and west. This is due to the "ghosting" effect mentioned in chapter 6, whereby the blocking circle used to determine the atmospheric transfer function can include blocking in the north and south directions, particularly where the phase speed is high. However, since the north/south atmospheric transfer functions is dependant on the east/west transfer functions, it cannot be trusted to produce realistic results independently. This is because the east/west blocking circles can become very large due to particularly strong winds in these directions. Hence, the fitting is only performed using east/west atmospheric transfer functions and the general all-directions transfer function.

The residual of the least squares fit to the observed gravity wave field can be extremely large when the fit is poor.[1] In order to make the finer scale differences discernible, the natural logarithm of the residual is taken.

7.2.1 Results

The log of the residuals as a result of fitting the tropopause gravity wave source function to the MF-radar derived MLT gravity wave climatology is shown in Figure 7.1. The vertical axis of this figure represents phase speeds from zero, while the colour scale of the graph represents the quality of the least squares fit. For instance, a dark blue area in April at $10ms^{-1}$phase

[1]Note, when the residual is referred to it is actually the norm of the residuals at each height bin.

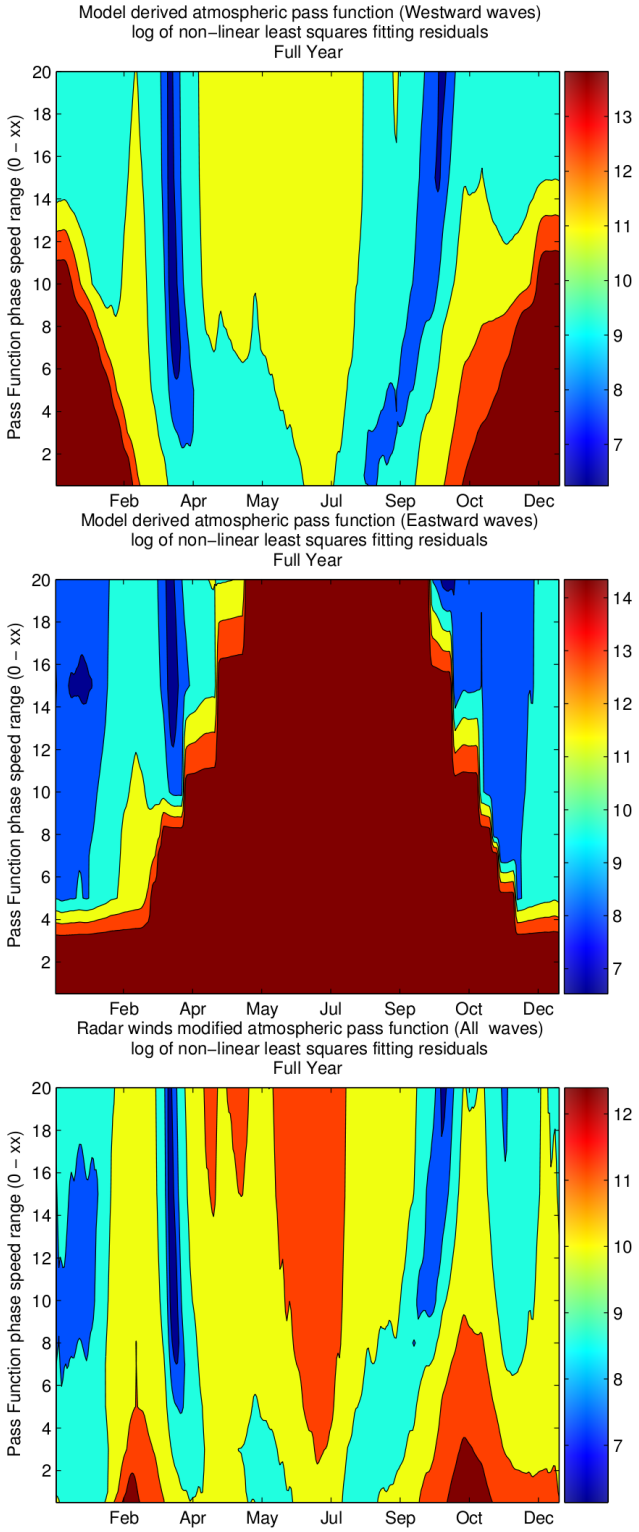

Figure 7.1: Log of residual fits of the tropopause source function (9-13km) and model wave passing field (with suitable exponential growth term) to the observed gravity wave field at 75-96km .

speed on the westward waves panel indicates that the radar derived gravity wave climatology is well described by waves with a phase speed between zero and $10ms^{-1}$propagating in the westward direction in April.

The effects of the polar night jet can be easily seen in the top two panels of Figure 7.1. The panel on the left shows that westward waves of a variety of phase speeds should be able to penetrate to the level observed by the radar (75 - $96km$). This is expected, since the strong eastward winds during the polar night cause critical level filtering of any eastward propagating waves. This effect can be seen in the right panel, where all eastward propagating waves are blocked regardless of phase speed. Note, however, that the above diagram only considers gravity waves with phase speeds no greater than $20ms^{-1}$. At some point gravity waves with sufficiently high phase velocities could be able to penetrate, although this would be rare.

The bottom panel in Figure 7.1 shows the log of the fitting residual using general gravity wave fitting, i.e. using the full blocking circle without restricting it to certain propagation directions. This gives a general overview of the possible gravity waves comprising the observed gravity wave field.

A feature in both the general gravity wave fitting case and the westward waves case is the relatively poor least squares fitting during the winter months. This may well be the result of year-to-year variability in the vortex, which would not be captured well by the HWM 93 model.

In order to examine this possibility further, the hybrid atmospheric transfer function calculated in Chapter 6 is used to least squares fit the atmospheric pass function and gravity wave source function to the observed gravity wave climatology. The hybrid atmospheric transfer function was an attempt to use real winds as measured by the Scott Base MF-radar to improve the model derived gravity wave filtering. The logged residual from the least squares fitting of this hybrid atmospheric transfer function, the tropopause source function and growth term to the radar gravity wave climatology is shown in Figure 7.2.

While the overall features of Figure 7.2 are similar to those of Figure 7.1, there is a significant difference in midwinter in both the westward wave blocking case (top left panel), and the general direction case (bottom panel). The lack of this winter feature for westward waves and the general wave case, gives some credence to the possibility that year-to-year variability, which would not be sufficiently captured by single year HWM 93 model, could have a significant effect on gravity waves in the winter months. The short time period over which the gravity wave climatology and hybrid transfer function are calculated could well be the factor that appears to reduce this winter feature in Figure 7.2.

Many papers have examined the effects of critical level filtering of gravity waves(see *Whiteway and Duck* (1996); *Baumgaertner and McDonald* (2007); *Dowdy et al.* (2007)). These studies show that during strong eastward winds eastward propagating gravity waves are filtered and visa versa for westward waves. These results are consistent with those obtained in this Chapter giving confidence in the use of least squares fitting residuals from fitting the atmospheric transfer function to the observed field as a method of determining wave blocking.

Interestingly the gravity wave source function appeared to have very little effect on the

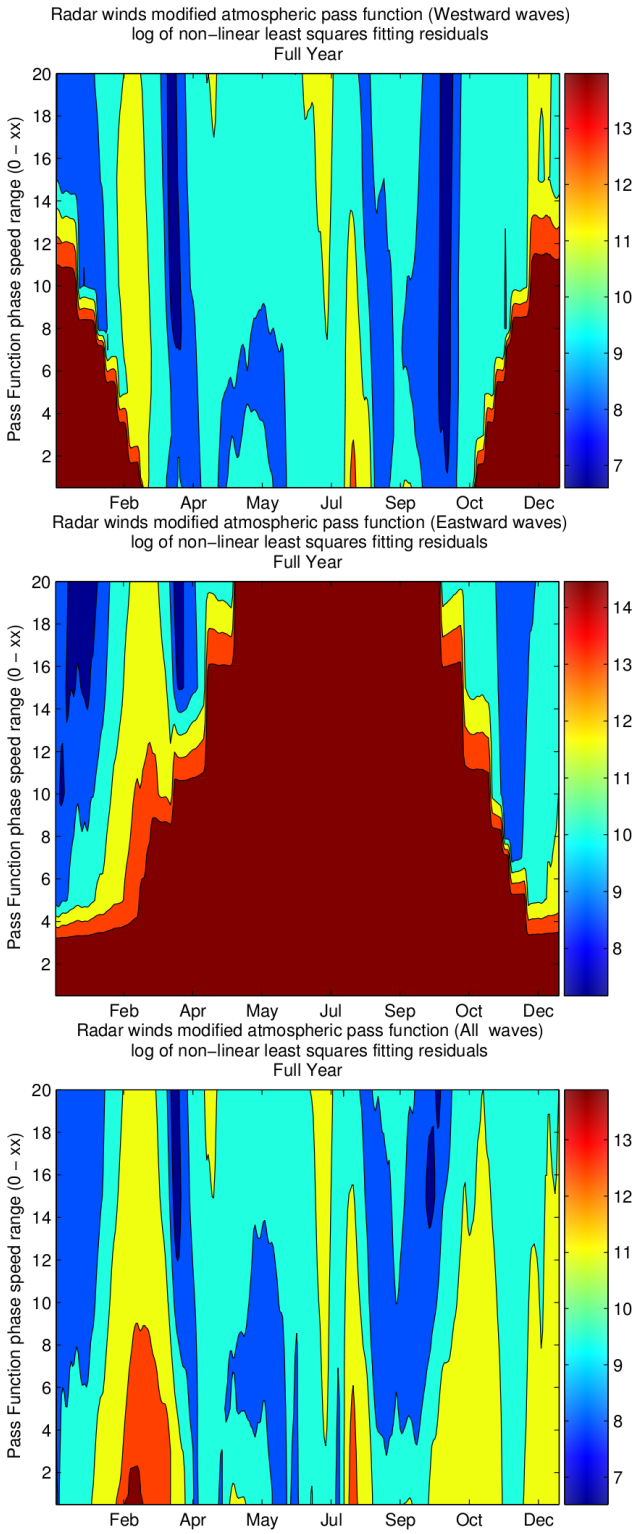

Figure 7.2: Log of residual fits of the tropopause source function (9-13km) and the radar modified wave passing field (with suitable exponential growth term) to the observed gravity wave field at 75-96km

least squares fitting residuals, it may be that the gravity wave field in the upper atmosphere is dominated by the filtering function to such an extent that the the source function had little influence on the observed field. However, it is also possible that by least squares fitting on each day of data, the fitting parameter in equation 7.2 may be overwhelming any possible effect from the source function. This is an effect which should be investigated in future. Performing the least squares fitting over a month may force the algorithm to account for the source function more.

Chapter 8

Summary and Discussion

This thesis set out to investigate the effects of gravity wave filtering above Scott Base, Antarctica. This was successful, in that the overall results matched with expectations based on previous studies.

Data from the Scott Base MF-radar system was used to develop a climatology of gravity wave activity over the period 2005 to 2008. This was a rather short period of time over which to base a climatology, selected because a radar data acquisition upgrade in late 2004 improved the radars data gathering rate. Despite the short timespan, the gravity wave climatology compares reasonably well to MF-radar derived gravity wave climatologies at other Antarctic sites(*Dowdy et al.*, 2007; *Hibbins et al.*, 2007). This provided enhanced confidence in the MF-radar gravity wave climatology.

Following the calculation of the MF-radar climatology, which spanned the mesosphere and lower thermosphere, a gravity wave climatology was produced for the troposphere and the region of the summer tropopause using radiosondes launched from McMurdo Station. This climatology was also afflicted by a short timespan of high quality data; analysis showed that data prior to late 2004 had a large average sampling height. This has been shown to introduce a strong observational bias when calculating gravity wave energy (*Alexander*, 1998). Because of this, the radiosonde data used for calculating the gravity wave source function was taken after the radiosonde program upgrade. Again, to test the validity of taking data over such a short time period, a climatology was produced using the lesser quality (but longer time period) data. Confidence in the post-upgrade data was gained by noting that the yearly variation in kinetic energy per unit mass for the new data was generally within one standard deviation of the previous data climatology.

Winds from the the Horizontal Winds Model 1993 (*Hedin et al.*, 1996) allowed the calculation of critical level filtering using blocking circles as defined by *Taylor et al.* (1993). Rather than examining a set of blocking circles to determine the degree and direction of filtering, the blocking circles were used to determine the fraction of waves blocked at a particular level. This was done by considering ranges of potential phase speeds from zero, and using Monte Carlo integration to determine what fraction of a circle gravity waves were blocked between certain phase speeds. This was used to create a model atmospheric transfer function by calculating the blocked fraction of gravity waves from the altitude gravity waves were assumed to propagate up from to $100km$. This resulted in a clear representation of

gravity wave filtering over Scott Base.

In order to test the model atmospheric transfer function, a similar transfer function was calculated by considering rotations of the wind vector. Rotation of the wind vector at 180 degrees between two altitudes would result in a low phase speed wave undergoing critical level filtering. This is only valid for low phase speed waves, however this analysis agreed well with the model atmospheric transfer function for low phase speed cases. This improved confidence in the model atmospheric transfer function.

The technique of using blocking circles to determine the fraction of gravity wave blocking does not appear to have been done in this way before. As such, this method could be useful in other locations. The atmospheric transfer function model was further extended by the use of a climatology of winds based on data from the Scott Base radar.

In Chapter 7 the atmospheric transfer function, the gravity wave source functions and an exponential term accounting for gravity wave growth with height were least squares fitted to the observed MLT gravity wave climatology. The residuals of this fit were used to determine the potential importance of the directional filtering of gravity waves. This chapter yielded several noteworthy results. It was determined that westward propagating waves contributed to the observed gravity wave field during winter while eastward propagating waves were most likely to contribute during the summer months (provided their phase velocity was not too low). These results are consistent with other papers which have investigated gravity wave filtering by critical levels (*Whiteway and Duck*, 1996; *Baumgaertner and McDonald*, 2007; *Dowdy et al.*, 2007). Additionally, it was determined that the gravity wave source function has very little effect on the final observed gravity wave field. However, it should be noted that this may well be an artifact of least squares fitting over each day as the fitting parameter would effectively change the magnitude of the source function at each day to best fit the observed data.

There are several ways in which techniques employed in this thesis could be improved in future. The most significant improvement would be the use of longer period high resolution data sets from both the MF-radar and radiosondes to improve their respective climatologies. This would provide more confidence in any results obtained and would also allow an analysis of the effect of year to year variability. An additional advantage of more year of high quality data would be the comparison of climatologies spanning the same period of time.

While the HWM 93 model was able to provide good data for an atmospheric transfer function, the hybrid atmospheric transfer function using radar winds appeared to give better results. For this reason a higher resolution model possibly like NCEP/NCAR reanalysis, but covering a larger range of altitudes would allow a more precise atmospheric transfer function to be calculated from the ground up. Lastly, it is possible that the least squares fitting algorithm was reducing the effect of the radiosonde derived source function by modifying it each day the fit was performed via the least squares fitting parameter. One way this effect could be mitigated would be to do the least squares fitting over a longer period of time, forcing the algorithm to account for daily variations in the source function.

Acknowledgments

Writing a thesis is tricky, and I would have been trickier without the following people.

Thanks to Adrian for his tireless hours of last-minute checking and comment-making, wealth of knowledge, taking me to Antarctica and being sneaky enough to have his office right across the hallway from mine so he could keep me on task ... or at least tense.

I would like to thank the many Grahames who have contributed to my work in such varied and sometimes surprising ways:

Grahame Frazier, my co supervisor for retaining my faith at the last minute - and of course assisting in supervising.

Grahame McDonald and Plank for all their work with the Birdlings radar upgrade, even though I didn't end up using it in my thesis, for van driving, ladder-holding and smack talking over the months of Birdlings trips.

Thanks to my office mates Rachel and Steve for helping me procrastinate and yet providing me with sound advice and help when I needed it

Thanks Euan for his comments, editing, crash courses in thesis writing and late night procrastination.

Thanks to Nikolai for his advice, editing, re-editing, re-re-editing, his amazing coffee machine of unparalleled awesome, and his continued assurance that socks with sandals is perfectly acceptable wear for postgrads - as long as it's at night "when no one else is around".

Thanks to my friends and family, especially Storm Geldenhuis and Joshua Collins for their many gifts of energy drinks, encouragement, smart-ass remarks....

Lastly thanks to my partner Rachel Bradstock for being totally awesome and helping to edit my thesis in spite of some pretty horrible grammar and spelling errors.

Bibliography

Alexander, M. J. (1998), Interpretations of observed climatological patterns in stratospheric gravity wave variance, *Journal of Geophysical Research*, *103*, 8627–8640.

Andreassen, C. E. Wasberg, D. C. Fritts, and J. R. Isler (1994), Gravity wave breaking in two and three dimensions 1. model description and comparison of two-dimensional evolutions, *J. Geophys. Res*, *99*, 8095–8108.

Andrews, D. G., J. R. Holton, and C. B. Leovy (1987), *Middle Atmosphere Dynamics*, International geophysics series, 489 pp., Academic Press, Orlando.

Baumgaertner, A., A. McDonald, and G. Fraser (2006), High resolution wind measurements in the mesosphere with the scott base medium-frequency radar.

Baumgaertner, A. J. G., and A. McDonald (2007), A gravity wave climatology for antarctica compiled from challenging minisatellite payload/global positioning system (champ/gps) radio occultations, *Journal of Geophysical Research*, *112*, doi:10.1029/2006JD007504.

Briggs, B. H. (1984), The analysis of spaced sensor records by correlation techniques, *Meteorology and Atmospheric Physics*, *13*, 166–186.

Buhler, O., and M. E. McIntyre (1999), On shear-generated gravity waves that reach the mesosphere. part ii: Wave propagation, *Journal of the Atmospheric Sciences*, *56*, 3764–3773.

Chapman, S., and R. S. Lindzen (1970), *Atmospheric Tides: Thermal and Gravitational*, 201 pp., Reidel, Dordrecht.

de la Torre, A., and P. Alexander (2005), Gravity waves above andes detected from gps radio occultation temperature profiles: Mountain forcing?, *Geophysical Research Letters*, *32*, L17,815 1–4.

Dean, S. M. (2002), Parameterisation of orographic cloud: A thesis submitted in partial fulfilment of the requirements for the degree of doctor of philosophy in physics at the university of canterbury, Doctoral, University of Canterbury.

Dowdy, A. J., R. A. Vincent, M. Tsutsumi, K. Igarashi, Y. Murayama, W. Singer, and D. J. Murphy (2007), Polar mesosphere and lower thermosphere dynamics: 1. mean wind and gravity wave climatologies, *Journal of Geophysical Research*, *112*, D17,104, doi: 10.1029/2006JD008126.

Fraser, G. (1984a), Summer circulation in the antarctic middle atmosphere, *Journal of Atmospheric and Terrestrial Physics*, *46*, 143–146.

Fraser, G. J. (1984b), Partial reflection spaced antenna wind measurements, in *International Council of Scientific Unions Middle Atmosphere Program, Vol. 13 p 233-247 (SEE N85-17452 08-46)*, vol. 13, pp. 233–247.

Fritts, D. C. (1978), The nonlinear gravity wave-critical level interaction, *Journal of the Atmospheric Sciences*, *35*, 397–413.

Fritts, D. C., and M. J. Alexander (2003), Gravity wave dynamics and effects in the middle atmosphere, *Reviews of Geophysics*, *41*, 3–1 3–64.

Fritts, D. C., J. R. Isler, and øyvind Andreassen (1994), Gravity wave breaking in two and three dimensions 2. three-dimensional evolution and instability structure, *Journal of Geophysical Research*, *99*, 8109?8124.

Garcia, R. R., and B. A. Boville (1994), "downward control" of the mean meridional circulation and temperature distribution of the polar winter stratosphere, *Journal of the Atmospheric Sciences*, *51*, 2238–2245.

Geller, M., H. Liu, J. Richter, D. Wu, and F. Zhang (2006), Gravity waves in weather, climate, and atmospheric chemistry: Issues and challenges for the community.

Geller, M. A. (1983), Dynamics of the middle atmosphere, *Space Science Reviews*, *34*, 359–375.

Gerbier, N., and M. Berenger (1961), Experimental studies of lee waves in the french alps, *Quarterly Journal of the Royal Meteorological Society*, *87*, 13–23.

Gill, A. E. (1982), *Atmosphere-ocean Dynamics*, International geophysics series, 662 pp., Academic Press, New York.

Goldberg, R. A. (1986), Middle atmosphere program. handbook for map, volume 19, in *Middle Atmosphere Program. Handbook for MAP, volume 19*, vol. 19.

Hamilton, K. (1999), Dynamical coupling of the lower and middle atmosphere historical background to current research, *Journal of Atmospheric and Solar-Terrestrial Physics*, *61*, 73–84, doi:10.1016/S1364-6826(98)00118-7.

Hedin, A. E., et al. (1996), Empirical wind model for the upper, middle and lower atmosphere, *Journal of Atmospheric and Terrestrial Physics*, *58*, 1421–1447, doi:10.1016/0021-9169(95)00122-0.

Hibbins, R., P. Espy, M. Jarvis, D. Riggin, and D. Fritts (2007), A climatology of tides and gravity wave variance in the mlt above rothera, antarctica obtained by mf radar, *Journal of Atmospheric and Solar-Terrestrial Physics*, *69*, 578–588, doi:10.1016/j.jastp.2006.10.009.

Hines, C. O. (1960), Internal atmospheric gravity waves at ionospheric heights, *Canadian Journal of Physics*, *38*, 1441–1481.

Hocking, W. K. (1997), Strengths and limitations of mst radar measurements of middle-atmosphere winds, *Annales Geophysicae*, *15*, 1111–1122, doi:10.1007/s00585-997-1111-1.

Holton, J. R. (1982), The role of gravity wave induced drag and diffusion in the momentum budget of the mesosphere, *Journal of the Atmospheric Sciences*, *39*, 791–799.

Holton, J. R., and M. J. Alexander (2000), The role of waves in the transport circulation of the middle atmosphere, *Geophysical monograph*, pp. 21–35.

Isler, J. R., D. C. Fritts, øyvind Andreassen, and C. E. Wasberg (1994), Gravity wave breaking in two and three dimensions 3. vortex breakdown and transition to isotropy, *Journal of Geophysical Research*, *99*, 8125?8138.

Kalnay, E., et al. (1996), The ncep/ncar 40-year reanalysis project, *Bulletin of the American Meteorological Society*, *77*, 437–471.

Kelley, M. C., and R. A. Heelis (1989), *The Earth's Ionosphere: Plasma Physics and Electrodynamics*, International geophysics series, 487 pp., Academic Press, San Diego.

Krutzmann, N. C., A. J. McDonald, and S. E. George (2008), Identification of mixing barriers in chemistry-climate model simulations using rényi entropy, *Geophysical Research Letters*, *35*, L06,806, doi:10.1029/2007GL032829.

Lindzen, R. S. (1981), Turbulence and stress owing to gravity wave and tidal breakdown, *Journal of Geophysical Research*, *86*, PAGES 9707?9714.

Makhlouf, U. B. (1989), *On the Role of Atmospheric Gravity Waves in Mesospheric Dynamics*, 60 pp., U.M.I, Ann Arbor, Mich.

Manson, A. H., and C. E. Meek (1984), Partial reflection d-region electron densities, in *International Council of Scientific Unions Middle Atmosphere Handbook, Vol. 13 p 113-123 (SEE N85-17452 08-46)*, vol. 13, pp. 113–123.

Namboothiri, S. P., A. H. Manson, and C. E. Meek (1993), E region real heights and their implications for mf radar-derived wind and tidal climatologies, *Radio Science*, *28*, 187–202.

Nastrom, G. D., and D. C. Fritts (1992), Sources of mesoscale variability of gravity waves. part i: Topographic excitation, *Journal of the Atmospheric Sciences*, *49*, 101–110.

Nastrom, G. D., A. R. Hansen, T. Tsuda, M. Nishida, and R. Ware (2000), A comparison of gravity wave energy observed by vhf radar and gps/met over central north america, *Journal of Geophysical Research*, *105*, 4685–4688.

Nicolet, M., and A. C. Aikin (1960), The formation of the d region of the ionosphere, *Journal of Geophysical Research*, *65*, PAGES 1469?1483.

Press, W. H. (1986), *Numerical Recipes: The Art of Scientific Computing*, 818 pp., Cambridge University Press, Cambridge [Cambridgeshire].

Ratnam, M. V., G. Tetzlaff, and C. Jacobi (2004), Global and seasonal variations of stratospheric gravity wave activity deduced from the champ/gps satellite, *Journal of the Atmospheric Sciences*, *61*, 1610–1620.

Read, P. L., and S. R. Lewis (2004), *The Martian Climate Revisited: Atmosphere and Environment of a Desert Planet*, Springer-Praxis books in geophysical sciences, 326 pp., Springer, Berlin.

Salby, M. L. (1996), *Fundamentals of Atmospheric Physics*, International geophysics series, 627 pp., Academic Press, San Diego.

Sato, K. (2000), Sources of gravity waves in the polar middle atmosphere, *Advances in polar upper atmosphere research*, *14*, 233–240.

Sato, K., T. Kumakura, and M. Takahashi (1999), Gravity waves appearing in a high-resolution gcm simulation, *Journal of the Atmospheric Sciences*, *56*, 1005–1018.

Sturman, A., and N. Tapper (2006), *The Weather and Climate of Australia and New Zealand*, 2nd ed ed., 541 pp., Oxford University Press, Melbourne.

Sutherland, B., and W. Peltier (1995), Internal gravity wave emission into the middle atmosphere from a model tropospheric jet, *Journal of the Atmospheric Sciences*, *52*, 3214–3235.

Taylor, M. J., E. H. Ryan, T. F. Tuan, and R. Edwards (1993), Evidence of preferential directions for gravity wave propagation due to wind filtering in the middle atmosphere, *Journal of Geophysical Research*, *98*, PAGES 6047?6057.

Tsuda, T., M. V. Ratnam, P. T. May, M. J. Alexander, R. A. Vincent, and A. MacKinnon (2004), Characteristics of gravity waves with short vertical wavelengths observed with radiosonde and gps occultation during dawex (darwin area wave experiment), *Journal of Geophysical Research (Atmospheres)*, *109*.

Vincent, R. A., and M. J. Alexander (2000), Gravity waves in the tropical lower stratosphere: An observational study of seasonal and interannual variability, *Journal of Geophysical Research*, *105*, PAGES 17,971?17,982.

Vincent, R. A., and D. C. Fritts (1987), A climatology of gravity wave motions in the mesopause region at adelaide, australia, *Journal of the Atmospheric Sciences*, *44*, 748–760.

Whiteway, J. A., and T. J. Duck (1996), Evidence for critical level filtering of atmospheric gravity waves, *Geophysical Research Letters*, *23*, 145–148.

Whiteway, J. A., T. J. Duck, D. P. Donovan, J. C. Bird, S. R. Pal, and A. I. Carswell (1997), Measurements of gravity wave activity within and around the arctic stratospheric vortex, *Geophysical Research Letters*, *24*, PAGES 1387?1390.

Yoshiki, M., and K. Sato (2000), A statistical study of gravity waves in the polar regions based on operational radiosonde data, *Journal of Geophysical Research*, *105*, 17,995–18,012.

Yoshiki, M., N. Kizu, and K. Sato (2004), Energy enhancements of gravity waves in the antarctic lower stratosphere associated with variations in the polar vortex and tropospheric disturbances, *Journal of Geophysical Research*, *109*, D23,104, doi:10.1029/2004JD004870.

Zangl, G., and K. P. Hoinka (2001), The tropopause in the polar regions, *Journal of Climate*, *14*, 3117–3139.

Zhong, Manson, Sonmor, and Meek (1996), Gravity wave exclusion circles in background flows modulated by the semidiurnal tide, *Annales Geophysicae*, *14*, 557–565, doi: 10.1007/s00585-996-0557-x.